Manuscript details

Manuscript number	IJMF_2016_188
Title	Bubble Collapse near a Fluid-Fluid Interface using the Spectral Element Marker Particle Method with Applications in Bioengineering
Article type	Research paper
Abstract	The spectral element marker particle (SEMP) method is a high-order numerical scheme for modelling multiphase flow where the governing equations are discretised using the spectral element method and the (compressible) fluid phases are tracked using marker particles. Thus far, the method has been successfully applied to two-phase problems involving the collapse of a two-dimensional bubble in the vicinity of a rigid wall. In this article, the SEMP method is extended to include a third fluid phase before being applied to bubble collapse problems near a fluid-fluid interface. Validation cases include time reversed three-phase rotation, three-phase Poiseuille flow, and two-phase bubble collapse near a rigid boundary (where a highly viscous third phase approximates the rigid boundary). In all cases good agreement is obtained with analytical solutions or previous numerical studies. A range of fluid parameter values and geometric configurations are studied before a bioengineering application is considered. A simplified model of (micro)bubble-cell interaction

	is presented, with the aim of gaining initial insights into the flow mechanisms behind sonoporation and microbubble-enhanced targeted drug delivery.
Keywords	bubble dynamics; drug delivery; sonoporation; spectral element; marker particle method; bioengineering
Corresponding Author	Christopher Rowlatt
Corresponding Author's Institution	The University of Manchester
Order of Authors	Christopher Rowlatt, Steven Lind

Submission files included in this PDF

File Type	File Name
Manuscript File	C-F-Rowlatt_S-J-Lind_IJMF-submission.pdf
Cover Letter	C-F-Rowlatt_S-J-Lind_Cover-Letter.docx

To view all the submission files, including those not included in the PDF, click on the manuscript title on your EVISE Homepage, then click 'Download zip file'.

Bubble Collapse near a Fluid-Fluid Interface using the Spectral Element Marker Particle Method with Applications in Bioengineering

Christopher F. Rowlatt[a,*], Steven J. Lind[a]

[a]*School of Mechanical Aerospace & Civil Engineering, The University of Manchester, Manchester, M13 9PL, United Kingdom.*

Abstract

The spectral element marker particle (SEMP) method is a high-order numerical scheme for modelling multiphase flow where the governing equations are discretised using the spectral element method and the (compressible) fluid phases are tracked using marker particles. Thus far, the method has been successfully applied to two-phase problems involving the collapse of a two-dimensional bubble in the vicinity of a rigid wall. In this article, the SEMP method is extended to include a third fluid phase before being applied to bubble collapse problems near a fluid-fluid interface. Validation cases include time reversed three-phase rotation, three-phase Poiseuille flow, and two-phase bubble collapse near a rigid boundary (where a highly viscous third phase approximates the rigid boundary). In all cases good agreement is obtained with analytical solutions or previous numerical studies. A range of fluid parameter values and geometric configurations are studied before a bioengineering application is considered. A simplified model of (micro)bubble-cell interaction is presented, with the aim of gaining initial insights into the flow mechanisms behind sonoporation and microbubble-enhanced targeted drug delivery.

Keywords: bubble dynamics, drug delivery, sonoporation, spectral element, marker particle method, bioengineering

1. Introduction

The dynamics of bubble collapse has received substantial attention in the literature over the past 100 years. Starting with Lord Rayleigh [1], who considered the collapse of a spherical cavity in an infinite expanse of incompressible fluid, subsequent experimental, numerical and analytical studies have highlighted a complex physical process, with jet formation, pressure shockwave emission, and torodial bubble formation possible (see, for example, [2, 3]). Research is motivated by the prevalence of bubbles in nature and industry and their fundamental role in many fluid systems.

*Corresponding author

Email addresses: christopher.rowlatt@manchester.ac.uk (Christopher F. Rowlatt), steven.lind@manchester.ac.uk (Steven J. Lind)

Cavitation damage due to bubble collapse is now a well-known phenomenon, and has negative consequences in a number of areas. In biomedicine, for example, ultrasound mediated drug delivery [4, 5, 6] and shock-wave lithotripsy procedures [7, 8], can generate cavitation bubbles that may cause cell death and hemorrhaging in the surrounding tissue, respectively. However, bubbles may also be used to dissolve blood clots (see e.g. [9]), break through the blood-brain barrier (see e.g. [10]) and clean and sterilise surfaces (see e.g. [11, 12]).

Numerical studies of bubble dynamics have been dominated by the boundary element method, originally used in this context by Blake and co-workers [13, 14]. The method requires the assumption of irrotationality, which considerably simplifies the governing equations. While this assumption has proven effective for moderate to high Reynolds numbers [15, 16, 17] and in cases of weak flow compressibility [18, 19], it precludes some key physics necessary in the modelling of multiphase biomedical flows, such as strong compressibility (i.e. ultrasound) and general non-Newtonian effects.

Numerical solutions of the full Navier-Stokes equations for bubble dynamics problems have received considerably less attention in the literature than boundary elements, most likely due to the increased implementation difficulty and computational time. Shopov *et al.* [20], Shopov and Minev [21] and Shopov *et al.* [22] considered a finite element approximation of the incompressible Navier-Stokes equations, where the mesh was fitted to the bubble surface and evolved in a Lagrangian manner. Fitting the computational mesh to the bubble surface could substantially increase the computational time, particularly under significant topological changes. Popinet and Zaleski [23] produced a well-defined (unfitted) interface over a finite volume grid by interpolating through bubble surface marker points using cubic splines. They found good agreement with experimental results for the incompressible phase of the dynamics but concluded that compressibility and thermal effects may be required for the compressible phase (bubble rebound).

Wang and Blake [18] developed an approximate theory for bubble dynamics in a compressible fluid using matched asymptotic expansions. The perturbation was performed to second order using the bubble-wall Mach number (assumed to be small). The bubble dynamics could then be numerically modelled using traditional boundary elements with compressibility appearing in the far-field boundary condition. Due to the assumption of a small Mach number, the method may not be able to accurately capture the bubble behaviour during the latter stages of collapse when larger degrees of compressibility may be required. However, excellent agreement was found with the Keller-Herring equation for spherical bubbles and test cases included the behaviour of a bubble under both a weak and strong acoustic wave. Wang [19] subsequently applied the compressible BEM model to bubble collapse near a rigid wall. During the incompressible phase of the bubble dynamics, Wang [19] achieved excellent agreement with experimental observations. During the bubble rebound, where compressibility is important, the agreement was an improvement on pre-

vious results (e.g. Popinet and Zaleski [23]) but still differed when compared to experiments (see their Fig. 8). It is likely that the secondary collapse phase required an amount of compressibility which is beyond the scope of the BEM model. In their boundary element study, Lee *et al.* [24] took a different approach and approximated compressible effects by incorporating a loss in energy (provided by experimental data) during the bubble rebound and found very good agreement with experimental results, including the capture of the elusive counterjet. Müller *et al.* [25] considered collapse of a gas filled bubble near a rigid wall using a finite volume technique for the *compressible* Euler equations. They showed that when a bubble collapses near a rigid wall (in the absence of viscosity, buoyancy and surface tension), the compressible bubble contents interact with reflected pressure shock-waves (caused by the oscillation of the bubble), producing vortices in the gaseous bubble contents. These vortices rotate in opposite directions and are directed towards the rigid wall. The vortices pull the gaseous bubble contents and bubble surface towards the rigid wall producing the well-known toroidal shape and high-speed liquid jet. Importantly, these are observations which cannot be obtained from incompressible and irrotational simulations such as BEM. The above studies, particularly that of Müller *et al.* [25], illustrate the importance of compressibility, even in situations commonly assumed to be predominantly incompressible. It is evident that if compressible effects are to be included then the full compressible Navier-Stokes (or Euler) equations must be considered.

Lind and Phillips developed a Spectral Element Marker Particle (SEMP) method for fully compressible bubble collapse problems in both Newtonian [26] and viscoelastic fluids [27] with small to moderate Reynolds numbers. SEMP uses the marker particle method [28] to track the fluid phases. The marker particle method is Lagrangian in nature and bears semblance to both the VOF [29] and the MAC [30] methods. A colour function C is determined by tracking massless marker particles. Each particle is assigned a particular colour depending upon the phase in which it resides, and because a particle of fluid will remain of that fluid type (assuming no change in phase), a particle will keep its colour indefinitely. Within fluid-fluid interface regions, where two (or more) differently coloured sets of marker particles reside, a weighted average is taken of the surrounding particles to determine an interpolated colour at a desired grid point. In this article, SEMP is extended to include a third (currently Newtonian) phase, that may be used to model deformable biological matter (e.g. cells or tissue). While there have been a number of works considering bubble collapse near deformable surfaces (see e.g. [16, 31]), few include sufficient physics to model the complex multiphase biomedical processes that motivate this work. Indeed, the eventual aim is to gain insights into the flow mechanisms behind sonoporation (e.g. [6]) and microbubble-enhanced targeted drug delivery (e.g. [5]).

This article is structured as follows. The mathematical model and governing equations are introduced in §2 with their numerical approximation discussed in §3. The three-phase method is

validated in §4 before a numerical investigation into the effect of viscosity and the thickness of the third phase is given in §5. A simplified model of (micro)bubble-cell interaction is presented in §6 before the article is concluded in §7.

2. The Mathematical Model and Governing Equations

Consider a two-dimensional (2D) domain Ω, which contains a gas-filled bubble Ω_b of initial density $\rho_{b,0}$, surrounded by fluid Ω_f of initial density $\rho_{f,0}$, placed near a fluid layer Ω_c such that $\Omega_f = \Omega \setminus (\Omega_b \cup \Omega_c)$. Note that all variables with index b will refer to those associated with the bubble, those labelled f with the ambient fluid and those labelled c with the fluid layer. A schematic is given in Fig. 1.

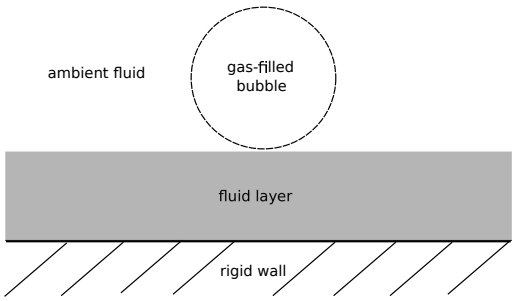

Figure 1: Schematic of the bubble Ω_b surrounded by an ambient fluid Ω_f and placed near a fluid layer Ω_c backed by a rigid wall.

In general, the equations governing fluid motion are the mathematical statements of conservation of momentum

$$\rho \frac{D\boldsymbol{u}}{Dt} = -\nabla p + \nabla \cdot \boldsymbol{S}, \tag{1}$$

and conservation of mass

$$\frac{D\rho}{Dt} + \rho \nabla \cdot \boldsymbol{u} = 0,$$

where $\boldsymbol{u}$ is the velocity, p is the pressure, $\boldsymbol{S}$ is the extra-stress tensor and ρ is the density. In the majority of bubble simulations in the literature (see e.g. [13, 23, 24, 17]), the fluid phases are assumed to be incompressible. However, in modelling bubble dynamics, particularly growth or collapse, one needs to account for the change in volume of the bubble, and so any fluid that may reside within must be modelled as compressible. Furthermore, and as discussed in the introduction, compressibility is known to play an important role in the final stages of bubble collapse, contributing significantly to energy dissipation [24]. Also, in the context of biomedical flows, if one requires accurate descriptions of any acoustic fields applied to or emitted from the bubble, compressibility and the complete conservation of mass equation must be retained. Accordingly, a thermodynamic equation of state is required to close the system of governing equations. Following

[26], the equation of state is taken to be the ideal gas law, namely

$$p = c^2 \rho, \tag{2}$$

where c is the speed of sound within the medium. Despite its simplicity, (2) is a useful model [26, 27]. Firstly, it provides a reasonably accurate thermodynamic description of the bubbles gaseous contents. Secondly, by variation of a *single* model parameter one can easily explore the effect of compressibility on the flow, and readily recover near-incompressibility, if required. The constitutive equation, or rheological equation of state, for a compressible Newtonian fluid is well known. The extra-stress tensor is given by

$$\boldsymbol{S} = \eta_1 \left(\nabla \boldsymbol{u} + \nabla \boldsymbol{u}^T \right) + \eta_2 \left(\nabla \cdot \boldsymbol{u} \right) \boldsymbol{I}, \tag{3}$$

where $\nabla \boldsymbol{u}$ is the velocity gradient, the superscript T denotes the transpose, $\boldsymbol{I}$ is the identity tensor and $\eta_{1,2}$ are scalar coefficients. Commonly, η_1 is named the (dynamic) shear viscosity coefficient and η_2 is termed the dilatational viscosity coefficient. Equation (3) is the most general constitutive equation for a Newtonian fluid as it imposes no restrictions on compressibility or on $\eta_{1,2}$. Often one abides by Stokes hypothesis and sets the bulk viscosity $\kappa = \left(\frac{2}{3}\eta_1 + \eta_2 \right)$ to zero [32]. As stated in [26], this implies that the mean mechanical pressure p^* becomes equivalent to the thermodynamic pressure p in Eqn. (1) and that the extra stress is trace free: $\sum_i S_{ii} = 0$. However, in this work Stokes' hypothesis is not adopted and the most general form of the compressible Newtonian extra-stress tensor (Eqn. (3)) is retained.

2.1. Nondimensionalisation of the governing equations

This article employs a similar nondimensionalisation as used in [26]: distances are scaled with respect to initial bubble radius R, densities are scaled with respect to the initial bubble density $\rho_{b,0}$, pressures are scaled with respect to $\rho_{b,0} V^2$, where V is a reference speed of sound (e.g. the speed of sound through an ideal gas), and stresses are scaled with respect to $\rho_{b,0} V^2$. Consequently, the nondimensional viscosities η^* are scaled according to

$$\eta^* = \frac{\eta}{\rho_{b,0} V R}.$$

A Reynolds number can be defined as $Re = 1/\eta^*$, but it is more beneficial to refer to nondimensional viscosities due to the several viscous parameters present in compressible models. Therefore, dropping the asterisks and substituting Eqn. (2) into Eqn. (1), the nondimensional governing equations for a compressible Newtonian fluid are: the conservation of momentum

$$\rho \frac{D\boldsymbol{u}}{Dt} = -c^2 \nabla \rho + \nabla \cdot \boldsymbol{S}, \tag{4}$$

the conservation of mass

$$\frac{D\rho}{Dt} + \rho \nabla \cdot \boldsymbol{u} = 0, \tag{5}$$

and the constitutive equation

$$\boldsymbol{S} = \eta_1 \left(\nabla \boldsymbol{u} + \nabla \boldsymbol{u}^T\right) + \eta_2 \left(\nabla \cdot \boldsymbol{u}\right) \boldsymbol{I}. \tag{6}$$

As in [26], a log-density formulation is implemented where the governing equations are solved for log density $q := \ln(\rho)$ and a kinematic stress $\boldsymbol{S} := \rho \boldsymbol{T}$. The standard and log-density formulations of the governing equations are physically equivalent, but the log-density formulation is convenient as the coupled mass and momentum equations become predominantly linear for constant kinematic viscosity [33, 34]. There are also numerical stability benefits for multiphase flows as potentially large density differences across interfaces are scaled down in magnitude when working with the log density. Accordingly, any subsequent reference to the density or stress will technically refer to the log density and kinematic stress, as defined above.

3. Numerical Solution of the Governing Equations

3.1. Time discretisation

In this article, a semi-Lagrangian approximation of the material derivative is used for both the conservation of momentum and mass equations (Eqns. (4),(5)), [33, 34]. A first-order Lagrangian approximation of the material derivative is

$$\frac{D\boldsymbol{u}}{Dt} \approx \frac{\boldsymbol{u}^{n+1}(\boldsymbol{x}^{n+1}) - \boldsymbol{u}^n(\boldsymbol{x}^n)}{\Delta t} = f(\boldsymbol{u}^{n+1}), \tag{7}$$

where $\boldsymbol{u}^n(\boldsymbol{x}) = \boldsymbol{u}(\boldsymbol{x}, t^n)$ is the velocity of a fluid particle $\boldsymbol{x}$ at time $t^n = n\Delta t$, $n = 1, \ldots, N_t$ (where N_t is the total number of time steps), $\boldsymbol{x}^n = \boldsymbol{x}(t^n)$ denotes the position of a fluid particle at time t^n and f is the right hand side of the momentum equation. Given $\boldsymbol{u}^n$, we wish to solve Eqn. (7) implicitly for $\boldsymbol{u}^{n+1}$ for each nodal point. Hence, in order to approximate the material derivative, the previous position $\boldsymbol{x}^n$ of the fluid particle that moves onto the nodal point $\boldsymbol{x}^{n+1}$ is required, in addition to the velocity $\boldsymbol{u}^{n+1}$. The velocity $\boldsymbol{u}^{n+1}$ and position $\boldsymbol{x}^{n+1}$ are found iteratively and further details of the algorithm used can be found in [26].

To summarise, the semi-discrete governing equations (in log-density formulation), which will shortly be discretised in space using the spectral element method, are given by: conservation of momentum

$$\frac{\boldsymbol{u}^{n+1} - \boldsymbol{u}^n}{\Delta t} = -c^2 \nabla q^{n+1} + \nabla \cdot \boldsymbol{T}^{n+1} + \nabla q^{n+1} \cdot \boldsymbol{T}^{n+1},$$

the conservation of mass

$$\frac{q^{n+1} - q^n}{\Delta t} + \nabla \cdot \boldsymbol{u}^{n+1} = 0,$$

and the constitutive equation

$$\boldsymbol{T}^{n+1} = \mu_1 \left(\nabla \boldsymbol{u}^{n+1} + (\nabla \boldsymbol{u}^{n+1})^T\right) + \mu_2 \left(\nabla \cdot \boldsymbol{u}^{n+1}\right) \boldsymbol{I},$$

where $\mu_{1,2} = \eta_{1,2}/\rho$.

3.2. Spectral Element Method

The spectral element method (SEM) was first proposed by Patera [35] to extend the application of spectral methods to problems defined in complex geometries. SEM has the geometric flexibility of a finite element method (FEM) with the accuracy of a spectral method and therefore, in principle is similar to *hp* - FEM. It is well-known that the SEM should perform better than traditional finite elements both in terms of accuracy and efficiency provided the solution is sufficiently regular and the accepted error level is sufficiently stringent [35].

3.2.1. Weak formulation

As stated at the beginning of this section, the whole domain $\Omega \subset \mathbb{R}^2$ contains the bubble Ω_b, the fluid layer Ω_c and the ambient fluid Ω_f such that $\Omega_f = \Omega \setminus (\Omega_b \cup \Omega_c)$. The spectral element method is based on solving the governing equations in their equivalent weak form. Thus, the dependent variables $\boldsymbol{u}$, q and $\boldsymbol{T}$ are chosen from the following function spaces:

$$\boldsymbol{u} \in \mathcal{V} := \left[H_0^1(\Omega)\right]^2, \quad q \in \mathcal{Q} := H^1(\Omega), \quad \boldsymbol{T} \in \mathcal{T} := \left[H^1(\Omega)\right]_s^{2\times 2},$$

where $H^1(\Omega)$ is a Sobolev space whose elements, and their first weak derivatives, are in $L^2(\Omega)$ [36], $H_0^1(\Omega)$ contains any elements of $H^1(\Omega)$ whose trace to the boundary $\partial\Omega$ is zero and $\left[H^1(\Omega)\right]_s^{2\times 2}$ contains all 2×2, symmetric tensors whose components are elements of $H^1(\Omega)$. Multiplying the strong form of the governing equations by an appropriate test function and integrating, yields the following semi-discrete weak formulation: find $(\boldsymbol{u}, q, \boldsymbol{T}) \in \mathcal{V} \times \mathcal{Q} \times \mathcal{T}$ such that

$$\int_\Omega \frac{\boldsymbol{u} - \boldsymbol{u}^n}{\Delta t} \cdot \boldsymbol{v} \, \mathrm{d}\Omega + \int_\Omega \boldsymbol{T} \colon \nabla \boldsymbol{v} \, \mathrm{d}\Omega = c^2 \int_\Omega q \nabla \cdot \boldsymbol{v} \, \mathrm{d}\Omega + \int_\Omega \nabla q \cdot \boldsymbol{T} \cdot \boldsymbol{v} \, \mathrm{d}\Omega \qquad \forall \boldsymbol{v} \in \mathcal{V}, \tag{8a}$$

$$\int_\Omega \left(\frac{q - q^n}{\Delta t} + \nabla \cdot \boldsymbol{u} \right) p \, \mathrm{d}\Omega = 0 \qquad \forall p \in \mathcal{Q}, \tag{8b}$$

$$\int_\Omega \boldsymbol{T} \colon \boldsymbol{W} \, \mathrm{d}\Omega - \int_\Omega \mu_1 \nabla \boldsymbol{u} \colon (\boldsymbol{W} + \boldsymbol{W}^T) \, \mathrm{d}\Omega = \int_\Omega \mu_2 (\nabla \cdot \boldsymbol{u}) \mathrm{tr}(\boldsymbol{W}) \, \mathrm{d}\Omega \qquad \forall \boldsymbol{W} \in \mathcal{T}, \tag{8c}$$

where $\mathrm{tr}(\boldsymbol{W})$ is the trace of a tensor.

3.2.2. Spatial discretisation

In the spatial discretisation of the weak formulation (8) using the spectral element method, it is necessary to choose conforming discrete subspaces $\mathcal{V}_N \subset \mathcal{V}$, $\mathcal{Q}_N \subset \mathcal{Q}$ and $\mathcal{T}_N \subset \mathcal{T}$. The domain Ω is divided into a number of non-overlapping, conforming, convex, quadrilateral spectral elements labelled $\Omega_{\alpha,\beta}$. The coordinates (α, β) label each spectral element such that $\alpha = 0, \ldots, \hat{\alpha}$ and $\beta = 0, \ldots, \hat{\beta}$. Thus, $\alpha_{max} = (\hat{\alpha} + 1)$ and $\beta_{max} = (\hat{\beta} + 1)$ denote the number of elements in the x and y directions respectively.

Let $P_N(\Omega_{\alpha,\beta})$ denote the space of all polynomials on $\Omega_{\alpha,\beta}$ of degree less than or equal to N and define:

$$\mathcal{P}_N(\Omega) := \left\{ \phi \colon \ \phi|_{\Omega_{\alpha,\beta}} \in P_N(\Omega_{\alpha,\beta}) \right\}$$

The velocity, density and stress approximation spaces may then be defined as:

$$\mathcal{V}_N := \mathcal{V} \cap [\mathcal{P}_N(\Omega)]^2, \quad \mathcal{Q}_N := \mathcal{Q} \cap \mathcal{P}_N(\Omega), \quad \mathcal{T}_N := \mathcal{T} \cap [\mathcal{P}_N(\Omega)]^{2\times 2}, \tag{9}$$

where it is understood that $[\mathcal{P}_N(\Omega)]^{2\times 2}$ defines each component of a tensor to be a member of $\mathcal{P}_N(\Omega)$. Note that the density and velocity approximation space are both of degree N. While compatibilty conditions for the velocity and pressure (not density) approximation spaces are known for incompressible flow, we emphasize that no inf-sup stability issues have been seen in our compressible computations. Each spectral element is mapped to the parent domain $D = [-1, 1] \times [-1, 1]$ using a transfinite mapping, $\boldsymbol{F}$, of Schneidesch and Deville [37], where for each point $\boldsymbol{\xi} = (\xi, \zeta) \in D$ there exists a point $\boldsymbol{x} = (x(\xi, \zeta), y(\xi, \zeta)) \in \Omega_{\alpha,\beta}$, such that $\boldsymbol{x} = \boldsymbol{F}(\boldsymbol{\xi})$ and the vertices of $\Omega_{\alpha,\beta}$ are given by $\boldsymbol{x}_1, \ldots, \boldsymbol{x}_4$. The velocity, density and stress are approximated on each element using Lagrangian interpolation through a select set of nodal points, called Gauss-Lobatto Legendre (GLL) points. In one dimension, the $(N+1)$ GLL points are roots of the polynomial $(1-\xi^2)L'_N(\xi)$ where L_N is the Legendre polynomial of degree N. Therefore, the Lagrange interpolant can be shown to take the form

$$h_i(\xi) = -\frac{(1-\xi^2)L'_N(\xi)}{N(N+1)L_N(\xi_i)(\xi-\xi_i)} \tag{10}$$

where ξ_i, $i = 0, \ldots, N$ are the GLL points. The Legendre polynomials are a subset of polynomial eigenfunctions (Jacobi polynomials) of the singular Sturm-Liouville differential operator and it is well known, that the expansion of a C^∞ function in terms of these eigenfunctions converges with spectral accuracy (exponential rates of convergence). Hence, an expansion in terms of the Lagrange interpolants (10) exhibits spectral properties, while also naturally lending itself to Gauss-Lobatto Legendre numerical quadrature. This is an improvement over traditional (h-type) finite element methods, which exhibit algebraic rates of convergence.

In 2D the GLL points form a $(N+1)^2$ grid within each element, interpolation over which yields the representation of each velocity component, stress component and density over the parent element

$$u^a(\xi, \zeta) = \sum_{i=0}^{N}\sum_{j=0}^{N} u^a_{i,j} h_i(\xi) h_j(\zeta), \tag{11a}$$

$$T^{a,b}(\xi, \zeta) = \sum_{i=0}^{N}\sum_{j=0}^{N} T^{a,b}_{i,j} h_i(\xi) h_j(\zeta), \tag{11b}$$

$$q(\xi, \zeta) = \sum_{i=0}^{N}\sum_{j=0}^{N} q_{i,j} h_i(\xi) h_j(\zeta), \tag{11c}$$

where $u^a_{i,j}$, $T^{a,b}_{i,j}$ and $q_{i,j}$ are the approximations to u^a, $T^{a,b}$ and q at each GLL point (ξ_i, ζ_j), respectively. For more details regarding the spectral approximation, the reader is referred to the monograph of Karniadakis and Sherwin [38].

The integrals in the weak form (8) are approximated using the Gauss-Lobatto Legendre quadrature rule

$$\int_{-1}^{1}\int_{-1}^{1} f(\xi,\zeta)\,\mathrm{d}\xi\mathrm{d}\zeta \approx \sum_{i=0}^{N}\sum_{j=0}^{N} f(\xi_i,\zeta_j)w_i w_j,$$

where the weights w_i are chosen so that the quadrature rule is exact for polynomials of degree less than or equal to $2N-1$ [39]. The fully discrete equations are then obtained by inserting the variable expansions (Eqns. (11)) into the weak form (Eqns. (8)) and applying the above quadrature rule. For details of the full discrete system, the reader is referred to [26].

3.3. The marker particle method

The marker particle method is a Lagrangian scheme to track multiple fluid phases and interfaces. A large number of particles placed within the domain act as *markers*, providing the identity of the fluid at a point in time and space. The approach was first suggested by Rider and Kothe [28] and compares favourably with VOF and level set methods. Particular benefits include the absence of numerical mass diffusion and numerical surface tension, and the ability to handle severe topological changes with ease. Furthermore, the scheme is straightforward to implement and is very robust [28]. It has been subsequently applied in Newtonian drop dynamics studies by Bierbrauer and Zhu [40] and Bierbrauer and Phillips [41], and the bubble dynamics studies of [26, 27].

The whole domain Ω is filled with initially equally spaced particles - a specified number per unit area. Every marker particle p is initially located at a unique position (x_p, y_p) and is assigned a colour, or identity, C_p^m defined by

$$C_p^m = \begin{cases} 1 & \text{if particle } p \text{ is in fluid } m, \\ 0 & \text{if particle } p \text{ is not in fluid } m. \end{cases} \tag{12}$$

Assuming no change in phase, particles initially of fluid m will remain so indefinitely and will be advected with fluid m. Hence, the colour function for each particle satisfies the advection equation, namely

$$\frac{DC_p^m}{Dt} = 0. \tag{13}$$

Eqn. (13) is ensured through the Lagrangian update of the marker particles. As the particles remain of fluid m, they can be assigned the constant material properties associated with fluid m, such as fluid viscosities μ_m.

3.3.1. Grid to particle interpolation

The marker particles, and hence the position of the relative phases, are updated using the velocities calculated on the Eulerian spectral element grid. The velocities are interpolated to each

marker particle, and the particles are advected with these velocities according to

$$\boldsymbol{u} = \frac{D\boldsymbol{x}}{Dt}.$$

The benefits of a spectral element formulation mean that internodal velocities can be found with ease and high accuracy using the Lagrange interpolant expansions (Eqn. (11a)). Therefore, a particle at (x_p, y_p) can be easily and accurately assigned a velocity $\boldsymbol{u}(x_p, y_p)$ and hence updated in position accordingly.

3.3.2. Particle to grid interpolation

The material properties of the fluids, carried with the marker particles, need to be projected onto the grid before solving the governing equations for the next time step. Following [26], material properties are assigned to each GLL node using the following averaging process:

$$\phi_{i,j} = \sum_{m=1}^{M} \phi^m C^m_{i,j}, \tag{14}$$

where ϕ^m denotes a material constant within fluid m (for example, viscosity) and M the total number of separate phases/fluids. Note that, in this article, we have three phases; the bubble, the adjacent fluid layer and the ambient fluid. The quantity $C^m_{i,j}$ is known as the interpolated colour function at the point (i, j) and is given by

$$C^m_{i,j} = \frac{\sum_{p=1}^{N_p} S(x_p - x_i, y_p - y_j) C^m_p}{\sum_{p=1}^{N_p} S(x_p - x_i, y_p - y_j)}, \tag{15}$$

where N_p is the total number of particles and S is a bilinear weighting function given by

$$S(x - x_i, y - y_j) = \begin{cases} \left(1 - \left|\frac{x-x_i}{\Delta x}\right|\right)\left(1 - \left|\frac{y-y_j}{\Delta y}\right|\right) & \text{if } 0 \le \left|\frac{x-x_i}{\Delta x}\right|, \left|\frac{y-y_j}{\Delta y}\right| \le 1, \\ 0 & \text{otherwise.} \end{cases} \tag{16}$$

Also, note that, by definition

$$\sum_{m=1}^{M} C^m_{i,j} = 1.$$

Although $C^m_{i,j}$ is found by summing over all particles in the domain (Eqn. (15)), only those within a square of area $4\Delta x \Delta y$ contribute to determining the interpolated colour function at GLL node (i, j). The interpolated colour function will be weighted towards the colour function (Eqn. (12)) of the majority of particles that are in close proximity to point (i, j). Consequently, by Eqn. (14), the material constants will be weighted toward those of the dominant fluid about (i, j). Of course, this is important only in regions near the interface where two distinct fluid types are present. Within the bulk of fluid $m = 1$, $C^1_p = 1$ whereas $C^2_p = C^3_p = 0$ for all particles p near (i, j). So $C^1_{i,j} = 1$ and $C^2_{i,j} = C^3_{i,j} = 0$; hence $\phi_{i,j} = \sum_{m=1}^{3} \phi^m C^m_{i,j} = \phi^1$.

We have some choice in specifying the size of the search square $4\Delta x\Delta y$. For regular finite difference meshes, Δx and Δy are taken to be the regular grid spacings. However, the GLL points are unequally spaced. Consequently, it seems prudent to leave the size of the search square as an independent parameter, which can be altered to suit the problem at hand, under the restriction that

$$\min\left(\Delta\xi_i\right) \leq \Delta x, \Delta y \leq \max\left(\Delta\xi_i\right), \tag{17}$$

where $\Delta\xi_i = |\xi_{i+1} - \xi_i|$, $i = 0, \ldots, N-1$ is the spacing between consecutive GLL points. In most instances, setting the search lengths $\Delta x, \Delta y$ to be an average of $\Delta\xi_i$ gives very reasonable results.

Note that throughout this article, we define additional marker particles $\boldsymbol{x}_{bot}$, $\boldsymbol{x}_{int}$, $\boldsymbol{x}_{top}$, which do not interact with the fluid in any way but are used solely to track the positions of the bottom and top of the bubble, as well as a point initially central on the interface between the ambient fluid and adjacent fluid layer.

3.3.3. Particle boundary conditions

It may be the case that particles near the boundary in the current time step may step outside the boundary in the next. To remedy this, the particles are simply reflected back into the domain by the amount at which they exceed it. This exact approach is used by Bierbrauer and Zhu [40] in their finite difference study and by [26].

4. Validation

In this section, the numerical method is validated using the case of three-phase time-reversed rotation, in addition to a three-phase Poiseuille flow example. Throughout this section, the following error measure for the phase mass is used:

$$E_M^m = \left|M_{exact}^m - M_{numeric}^m\right|, \tag{18}$$

where M_{exact}^m and $M_{numeric}^m$, are given by

$$M_{exact}^m = \int_{\Omega^m} \mathrm{d}\Omega, \qquad M_{numeric}^m = \int_{\Omega} C^m \,\mathrm{d}\Omega$$

Note that the fluid phases are identified by $m = 1, 2, 3$. Additionally, for the steady state three-phase Poiseuille flow example considered in §4.2, the error of the velocity profile with respect to the maximum norm is also used to validate the SEMP method:

$$\left\|\boldsymbol{u} - \boldsymbol{u}_N\right\|_\infty = \max_{\boldsymbol{x}\in\Omega} \left|\boldsymbol{u}(\boldsymbol{x}) - \boldsymbol{u}_N(\boldsymbol{x})\right| \tag{19}$$

where $\boldsymbol{u}$ and $\boldsymbol{u}_N$ are the analytical and computed velocity profiles, respectively.

4.1. Time Reversed Rotation

Although the marker particle method has been validated for two-phase simulations (Lind and Phillips [26]), the presence of an additional phase makes it necessary for re-validation. Let $\Omega = [0,1]^2$ contain an initially circular bubble with radius $R = 0.15$ and centre $\boldsymbol{x} = (0.5, 0.75)$, with an adjacent fluid layer $\Omega_c = [0,1] \times [0, 0.1]$. The initial configuration is depicted in Fig. 2a. The fluid is then advected according to a velocity field $\boldsymbol{u}(\boldsymbol{x}, t)$, whose time-dependent components are given by

$$u(x,y,t) = -\sin(2\pi y)\sin^2(\pi x)\cos\left(\frac{\pi t}{T}\right), \tag{20a}$$

$$v(x,y,t) = \sin(2\pi x)\sin^2(\pi y)\cos\left(\frac{\pi t}{T}\right), \tag{20b}$$

where $t \in [0,T]$ and T is the final time of the simulation. The velocity field (20) will reverse at time $t = T/2$ and return to its initial position at $t = T$. An illustration of the deformation undergone by both the bubble and the fluid layer, at $t = T/2$, is depicted in Fig. 2b.

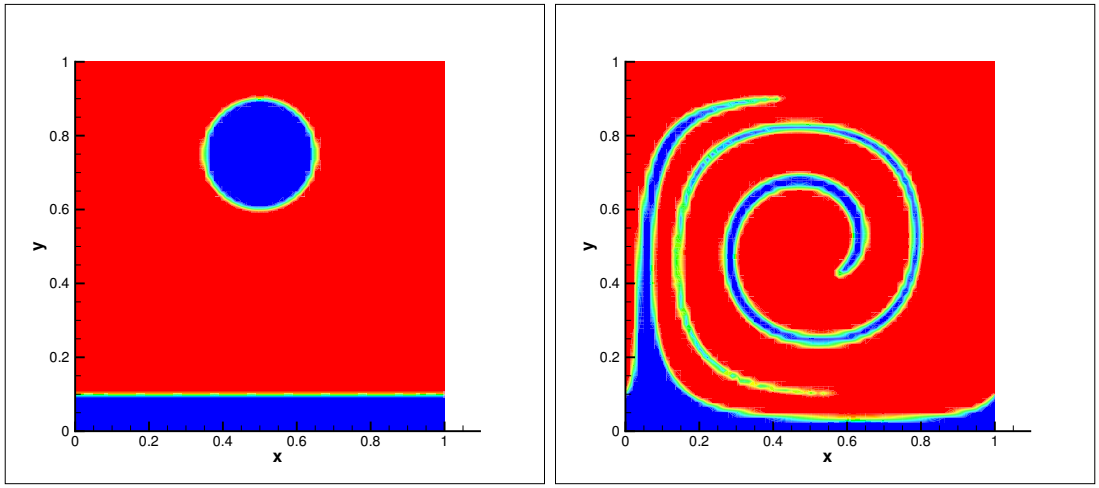

(a) $t = 0$ **(b)** $t = T/2$

Figure 2: Colour function for time reversed rotation example at $t = 0$ and $t = T/2$.

There are two ways to increase the marker particle density; increasing the number of particle cells in each direction (N_x, N_y) (akin to h-refinement), or increasing the number of particles-per-cell $\hat{N}_p$ (akin to p-refinement). The minimum distance between Gauss-Lobatto Legendre points scales with $\mathcal{O}(1/N^2)$, approximately. Therefore, when $N = 10$, we require $N_x, N_y \leq 100$ so that Eqn. (17) is satisfied. Thus, we set $N_x = N_y = 100$ and consider increasing the marker particle density by increasing $\hat{N}_p$.

Table 1 shows the error in the mass at the end of the simulation, $t = T$, for a single mesh with increasing marker particle density, and for each phase $m = 1, 2, 3$. It is evident that increasing the marker particle density improves the mass error with approximate linear convergence seen in

most cases. This is a satisfactory result, especially given the highly complex three phase distortion observed for this test case.

N_p	E_M^m		
	$m=1$	$m=2$	$m=3$
301^2	1.17×10^{-4}	1.64×10^{-3}	1.52×10^{-3}
401^2	1.76×10^{-4}	1.32×10^{-3}	1.14×10^{-3}
501^2	9.94×10^{-5}	1.01×10^{-3}	9.13×10^{-4}
601^2	4.56×10^{-5}	8.09×10^{-4}	7.63×10^{-4}

Table 1: Error in the mass for a single mesh ($N = 10$, $\alpha_{max} = 10$, $\beta_{max} = 10$) for each phase $m = 1, 2, 3$.

4.2. Multiphase Poiseuille Flow

In this section, the three-phase spectral element marker particle method (SEMP) is validated using a steady state Poiseuille flow example. Consider three immiscible, incompressible fluids flowing in the x direction in a horizontal thin slit of length L and height H under the influence of a horizontal pressure gradient $\partial p/\partial x = P$. Thus, we define our domain $\Omega = [0, L] \times [0, H]$, which contains three distinct phases:

$$\Omega_1 = [0, L] \times [0, a], \quad \Omega_2 = [0, L] \times [a, b] \quad \text{and} \quad \Omega_3 = [0, L] \times [b, H],$$

where $a = H/3$ and $b = 2H/3$. Note that throughout this subsection, $L = 10$ and $H = 5$. The liquid phases are flowing sufficiently slowly so that the fluid-fluid interfaces remain planar. Note that as the analytical solution assumes incompressibility, the speed of sound is increased to a very large value ($c^2 = 10^9$), and the dilatational viscosity given in (3) is set to zero. Each fluid phase is assumed to have distinct dynamic viscosities, defined as: η_1, η_2 and η_3, where the subscripts are not to be confused with the subscripts in (3). The analytical solution for two-phase steady state Poiseuille flow is given by Bird *et al.* [42]. However, in the absence of a three-phase steady state Poiseuille flow solution, the authors have provided a derivation which is available in the Appendix A.

In this section, we set $c^2 = 10^9$, $\mu_1 = 5$, $\mu_2 = 1$ and $\mu_3 = 8$ and run the simulation for $10,000$ time steps with a time step length $\Delta t = 10^{-4}$, so that $T = 1$. A uniform, quadrilateral mesh is employed in this section with parameters $\alpha_{max} = 10$, $\beta_{max} = 10$ and $N = 8, 10$. The initial and boundary conditions for the velocity field are taken to be the analytical solution. For the viscosities considered in this section, Figs. 3a and 3b illustrate the analytical and computed u components of the velocity field at the end of the simulation, respectively, when $N = 10$. Clearly good qualitative agreement is seen between the analytical and computed velocity solutions. The

contour plots are the magnitudes of the v component of the velocity field. The analytical v component should be identically zero, as can be seen in Fig. 3a. However, it is clear from Fig. 3b, that the computed solution contains small non-zero contributions to the v component around the interface between the phases. The non-zero v component in the computed solution is an error introduced by the smoothing of the material parameters across the interface between phases which, theoretically, contains a weak discontinuity (due to different viscosities). This error is an unavoidable consequence of adopting a "one field" model, but is clearly small in magnitude ($\approx 2\times10^{-2}$) and little cause for concern. For this case the error in the maximum norm (Eqn. (19)) between the analytical and computed velocity solutions, at the end of the simulation, is found to be approximately 9.0×10^{-2}. This is a suitably small value that is found to be quite insensitive to moderate changes in resolution (e.g. when $N = 8, 10$ or $100 \leq N_x \leq 140$ and $60 \leq N_y \leq 80$ in various combinations). Indeed, the smoothing of material parameters in this one field model limits convergence when measured against a test case with a weak discontinuity in the analytical solution. Nevertheless, the maximum error in the simulation is small enough in magnitude to deem the three-phase SEMP method validated.

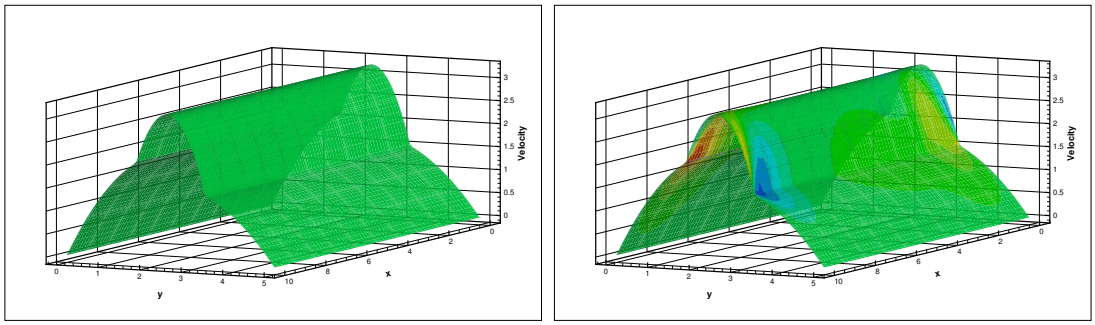

(a) Analytical **(b)** Computed

Figure 3: Comparison between the analytical and computed solutions, at the end of the simulation $t = T = 1$, when $\mu_1 = 5$, $\mu_2 = 1$, $\mu_3 = 8$ for $N = 10$. The solution is the u component of the velocity field, whilst the contour is the v component.

4.3. Two-phase example

Finally, we validate the bubble dynamics by considering a three-phase approximation to a two-phase example: bubble collapse near a rigid wall. This is accomplished by setting the fluid layer to have a high viscosity so that it approximates the rigid wall. This setup should obtain results that are in close qualitative agreement with the two-phase examples published by Lind and Phillips [26]. Throughout this section, let $\Omega = [0, 10]^2$ contain an initially circular bubble, with radius $R = 1$ and centre $\hat{\boldsymbol{x}} = (5.0, 2.2)$ and a fluid layer $\Omega_c = [0, 10] \times [0, 1]$. We use the same parameters as those chosen by Lind and Phillips [26]; that is, the bubble has density $\rho_{b,0} = 0$ and viscosity $\mu_b = 10^{-5}$, while the ambient fluid has density $\rho_{f,0} = \ln(4)$ and viscosity $\mu_f = 10^{-2}$.

The fluid layer density is given by $\rho_{c,0} = \rho_{f,0}$ whilst the viscosity is $\mu_c = 10^3$. The simulations were run until $T = 10$ with a time step length $\Delta t = 5 \times 10^{-3}$. The mesh used for both of the examples in this section is the same as the one used by Lind and Phillips [26] and is depicted in Fig. 4a, where $N = 8$, $\alpha_{max} = \beta_{max} = 9$. The initial configuration of this test case is shown in Figure 5a.

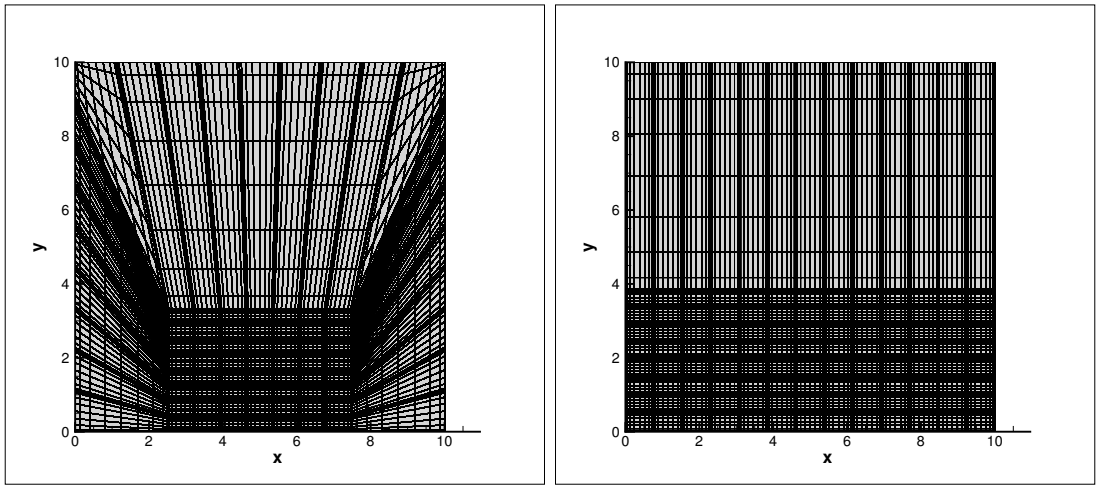

(a) Mesh 1 **(b)** Mesh 2

Figure 4: Illustration of (a) Mesh 1; the refined region is a box local to the bubble and (b) Mesh 2; the refined region is a strip, which contains both the bubble and the fluid-fluid interface.

Figure 5b illustrates the colour function at the end of the simulation $t = T = 10$. Clearly, a broad jet has formed which impinges on the fluid layer and pushes the bubble contents out towards the side walls. Even though the viscosity of the fluid layer is very high, the centre of the fluid layer interface does move slightly upwards as the simulation progresses. Nevertheless, the results are in good qualitative agreement with the two-phase results of Lind and Phillips [26] depicted in Fig. 5c.

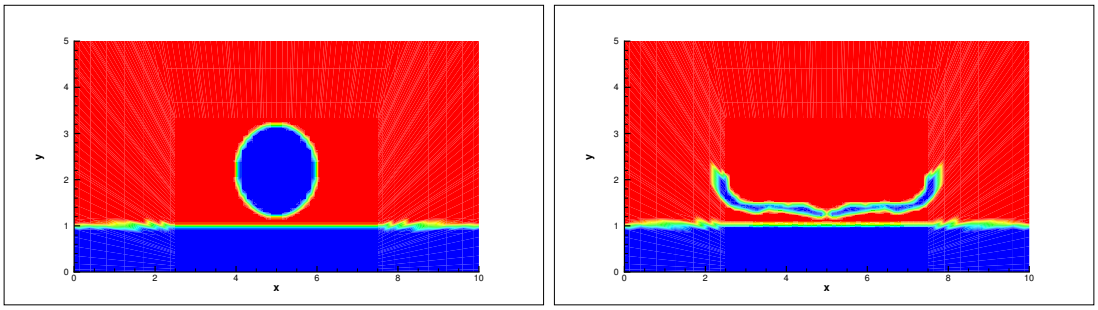

(a) Initial configuration, $t = 0$ **(b)** Final configuration, $t = 10$

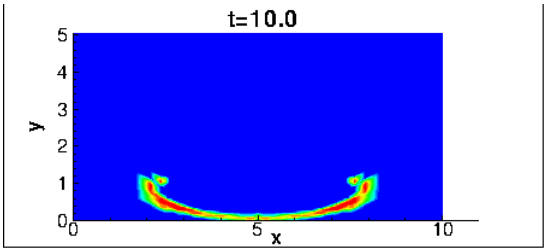

(c) Lind and Phillips [26] colour function at $t = 10$
(reprinted with permission from the authors)

Figure 5: Colour function at (a) the beginning, (b) the end of the simulation and (c) two-phase results of Lind and Phillips [26] (reprinted with permission from the authors).

5. Numerical Investigation

This section is dedicated to the numerical investigation of the collapse of a gas-filled bubble near a fluid-fluid interface with a rigid backing, where both the ambient fluid and the fluid layer are Newtonian. As mentioned in the introduction, the SEMP method was developed for flows with small to moderate Reynolds number, or equivalently, when the density difference across phases is small. To the authors' knowledge, these are the only results (experimental or numerical) for low inertia bubble collapse near a fluid-fluid interface backed by a rigid wall. As mentioned, in the interests of clarifying the effect of key parameters on dynamics, this study focuses primarily on the effect of viscosity, and accordingly omits any effects due to applied ultrasound, buoyancy or surface tension. Firstly, we demonstrate that the bubble dynamics do not change under a p-refinement over a reasonable physical time ($O(1)$ time units). Then we consider variations in both the ambient fluid viscosity and the fluid layer viscosity by separating the results into two parts: when the ambient fluid viscosity is less than the fluid layer viscosity, $\mu_f < \mu_c$ and vice-versa, $\mu_f > \mu_c$. Finally, we consider the influence the rigid backing has on the collapse.

Throughout this section, the domain $\Omega = [0, 10] \times [0, 10]$ contains a gas-filled bubble, Ω_b, and a fluid layer, Ω_c, so that the ambient fluid occupies the domain $\Omega_f = \Omega \setminus (\Omega_b \cup \Omega_c)$. With the exception of §5.4, the bubble centre is positioned at $\bar{\boldsymbol{x}} = (5, 2.2)$ with an initial radius $R = 1$. The bubble's contents are modelled as a compressible fluid with density $\rho_{b,0} = 0$ and a constant

viscosity $\mu_b = 1 \times 10^{-5}$. The fluid layer occupies the domain $\Omega_c = [0, 10] \times [0, h]$, where a height $h = 1$ is assumed in all subsections except §5.4, and has the same density as the ambient fluid, i.e. $\rho_{c,0} = \ln(4) = \rho_{f,0}$. The time step length is given by $\Delta t = 5 \times 10^{-3}$. We define three special marker particles which track the top and bottom of the bubble as well as the centre of the interface between the ambient fluid and the fluid layer. These marker particles are denoted by $\boldsymbol{x}_{top}$, $\boldsymbol{x}_{bot}$ and $\boldsymbol{x}_{int}$, respectively.

5.1. Mesh Choice

In this section, a p-refinement study of Mesh 2 (depicted in Fig. 4b) is undertaken for a bubble placed near a fluid layer. Similarly to §4.3, the simulation is run until $t = T = 10$ with a time step length $\Delta t = 5 \times 10^{-3}$.

For viscosities $\mu_f = 10^{-1}$, $\mu_c = 1.0$, the mesh demonstrates near independence in the position markers with p-refinement for long physical times (see Fig. 6a). This helps to confirm that for parameter values of this order, long simulations may be run with some confidence in the accuracy of the results. For an ambient fluid viscosity some two orders of magnitude smaller $\mu_f = 10^{-3}$, converged solutions are obtained over a shorter timescale, with near independence in p-refinement demonstrated up to $t = 1$ (see Fig. 6b). Beyond this, results lose grid independence, as small scale perturbations in the bubble surface, which are sensitive to grid resolution, grow undamped by any viscous or surface tension effects. Accordingly, in any forthcoming cases where $\mu_f = 10^{-3}$, the physical time of $t = 1$ will be deemed the approximate limit for reliable, grid independent solutions. This restriction at lower viscosity has little impact on the applicability of the method as it is often the case (at lower viscosities) that the most interesting and important bubble dynamics are at the start of the growth/collapse process, before any potential steady states are reached.

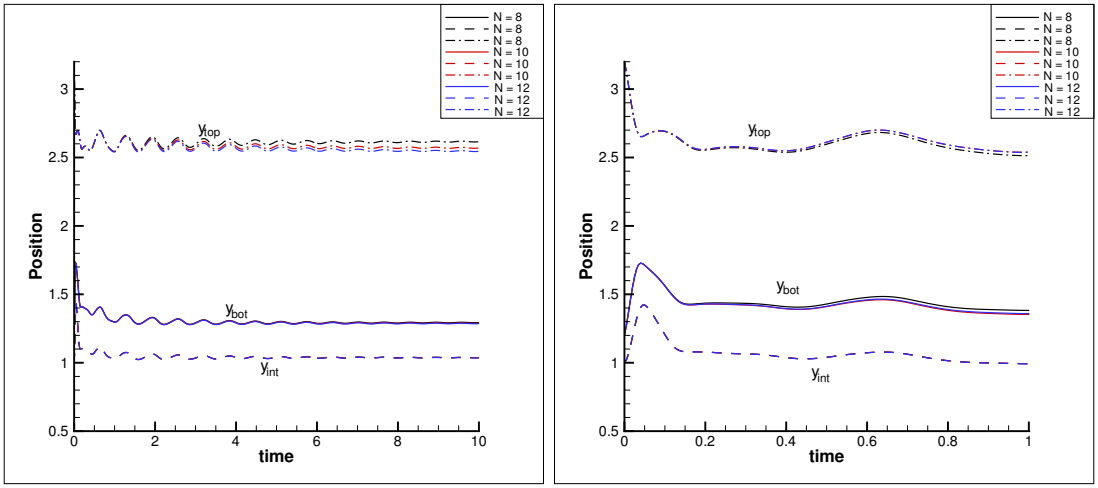

(a) $\mu_f = 10^{-1}$ **(b)** $\mu_f = 10^{-3}$

Figure 6: y coordinate of the position of the markers particles $\boldsymbol{x}_{bot}$, $\boldsymbol{x}_{int}$ and $\boldsymbol{x}_{top}$ in time for $\mu_c = 1.0$ using (a) $\mu_f = 10^{-1}$ and (b) $\mu_f = 10^{-3}$ when $\alpha_{max} = \beta_{max} = 9$ and $N = 8, 10, 12$.

Note that over the time scales considered in subsequent sections of this article, the solutions also displayed mesh independence between Mesh 1 and Mesh 2 (depicted in Fig. 4). However, the comparison is not included here in the interests of brevity.

5.2. Ambient Fluid Viscosity less than Fluid Layer Viscosity

In this section we consider the case where the ambient fluid viscosity is less than the viscosity of the fluid layer. In this section we restrict ourselves to the time period $t = 0, \ldots, 0.5$, because, as indicated previously, the most interesting dynamics seem to occur within this period.

Fig. 7 illustrates the colour function at times $t = 0.04, 0.08, 0.12, 0.16, 0.2$ and 0.5 for material parameters $\mu_f = 10^{-3}$ and $\mu_c = 10^{-1}$. The initial configuration is the same as depicted in Fig. 5a. At $t = 0.04$, the bubble has collapsed spherically and has clearly drawn the fluid-fluid interface upwards to the bubble. It will be shown later, that this initial collapse phase is controlled primarily by the pressure difference between the bubble and ambient fluid, with very little dependence on viscosity. The bubble then goes through an expansion phase which can be seen at $t = 0.08$. This expansion pushes the centre of the fluid-fluid interface downwards slightly before the bubble is elongated towards the fluid-fluid interface, which can be seen at $t = 0.12$. This elongation is commonly seen in bubble cavitation problems and may be accompanied by jet formation. No jet is seen here, however, due to rapid equilibration of pressures inside and outside the bubble after the initial collapse. The elongation of the bubble occurs due to a Bjerknes-style migration of the bubble (towards the more rigid layer). This migration causes the layer to compress slightly and then rebound, flattening the underside of the bubble at $t = 0.16$ and 0.2. From then on, the bubble dynamics approach a steady state, with no significant temporal change in dynamics.

Small perturbations can be seen in the bubble surface at $t = 0.5$. As mentioned, these arise due to an absence of surface tension, but may evolve into un-physical flow features at later times as their small scale is under-resolved by the grid. For larger viscosity values, these perturbations are dampened entirely (see Fig. 8) with long-term stability evident, as demonstrated in Fig. 6a.

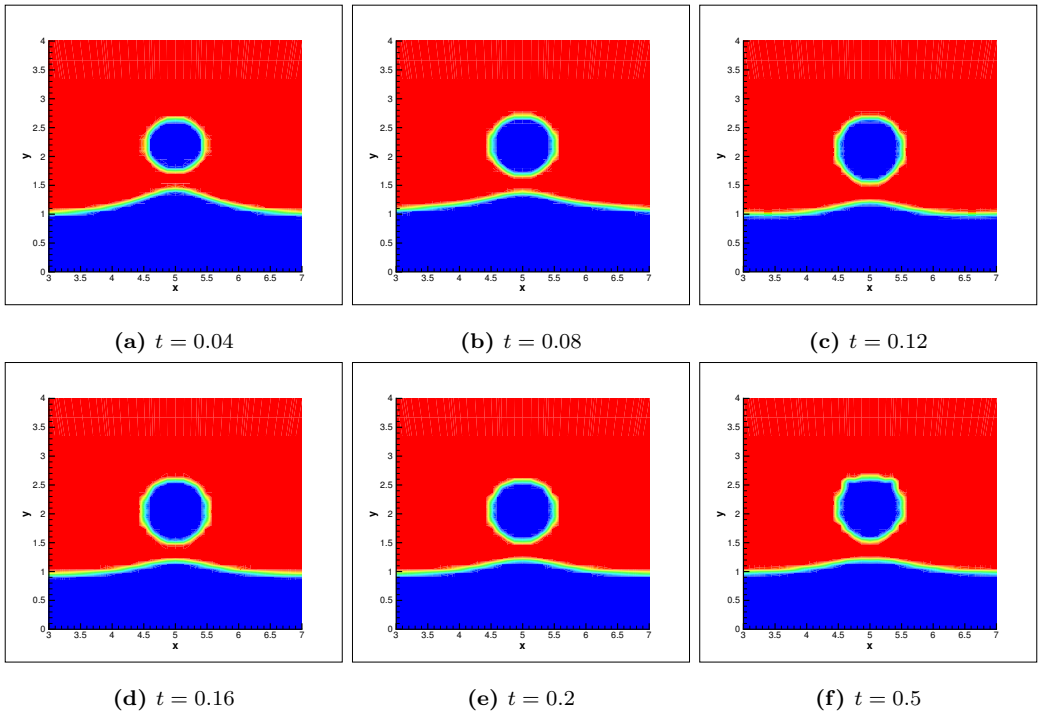

(a) $t = 0.04$ **(b)** $t = 0.08$ **(c)** $t = 0.12$

(d) $t = 0.16$ **(e)** $t = 0.2$ **(f)** $t = 0.5$

Figure 7: Colour function for $\mu_f = 10^{-3}, \mu_c = 10^{-1}$ at various points in time.

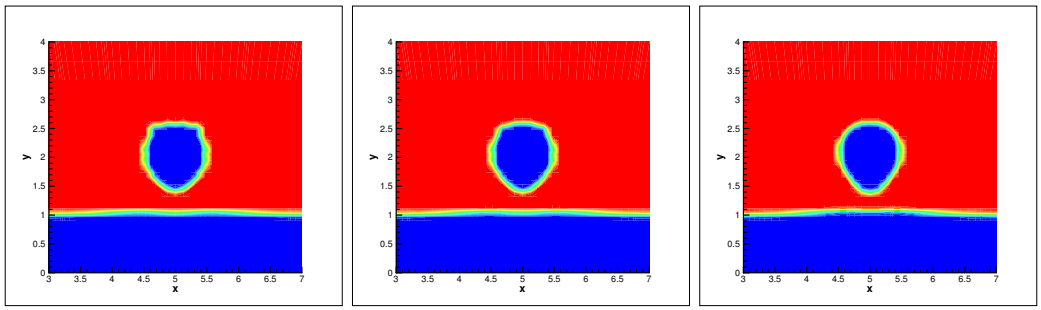

(a) $\mu_f = 10^{-3}$ **(b)** $\mu_f = 10^{-2}$ **(c)** $\mu_f = 10^{-1}$

Figure 8: Colour function for $\mu_f = 10^{-3}, 10^{-2}, 10^{-1}$, $\mu_c = 1.0$ when $t = 0.5$.

Fig. 9 illustrates contours of the streamline normal stress at times $t = 0.04, \ldots, 0.5$. This stress is defined as the component of the Cauchy stress parallel to instantaneous streamlines, and provides a geometrically invariant measure of the normal stress in the direction of the flow [34]. It is clear that the majority of normal stress occurs in the fluid layer region. In this article, we do not

include the action of external forces such as gravity and therefore, the evolution of normal stress is caused solely by the bubble dynamics. At $t = 0.04$, a localised peak normal stress can be seen in the central bump in the fluid-fluid interface, before spreading throughout the fluid layer. Although this stress seems to dissipate as the simulation progresses, the fact that the stress is largest and highly localised in the early stages of dynamics has potential implications in biomedicine: if the fluid layer represents a cell or tissue layer, depending on the mechanical properties and biological response, this could be indicative of regions of damage or even cell death. It is also evident that, as the simulation progress, the largest magnitudes of stress are seen at the rigid wall. We investigate the influence of the rigid wall later in the article, but note this may have significant implications for bubble cleaning processes (if the fluid layer were to be a model of some unwanted material deposit or contaminant).

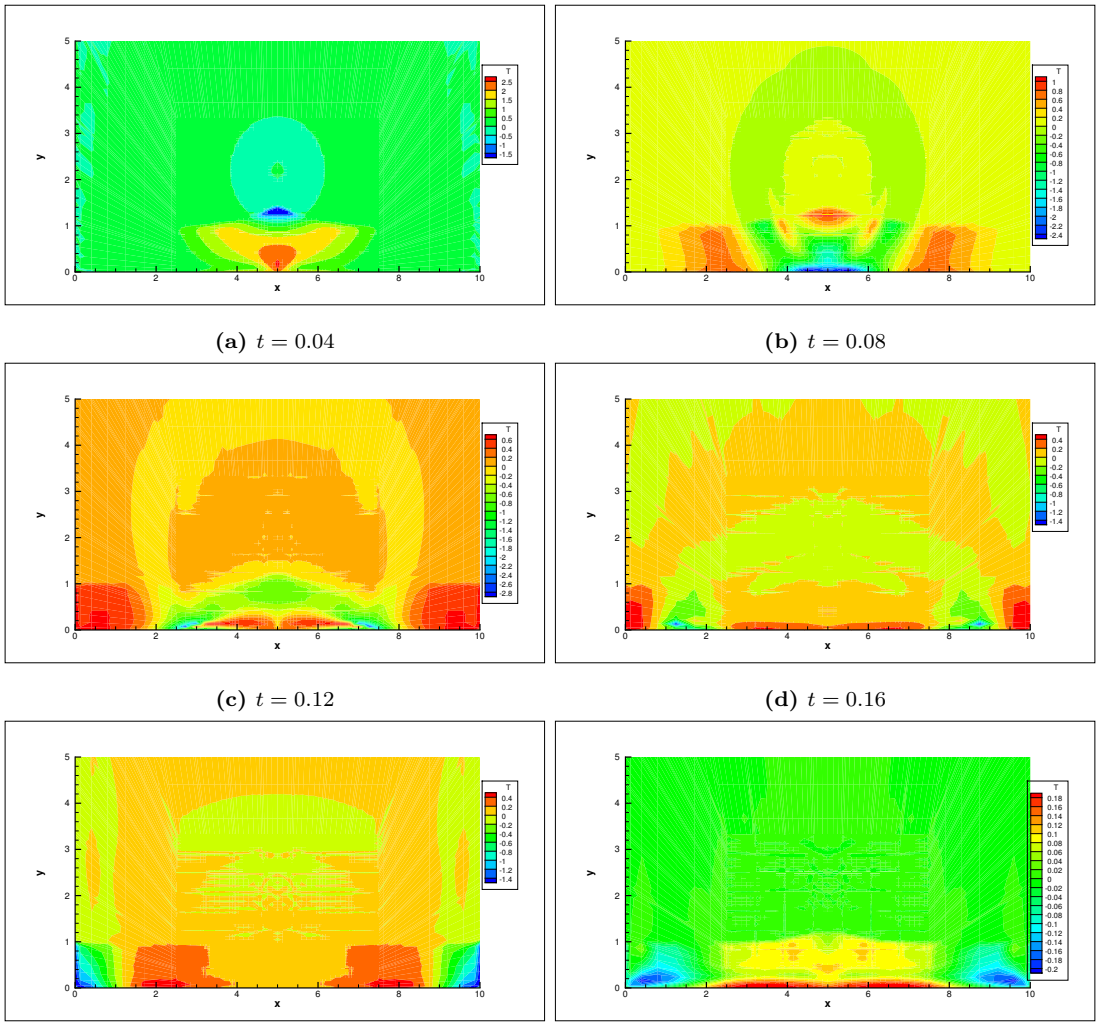

(a) $t = 0.04$ **(b)** $t = 0.08$

(c) $t = 0.12$ **(d)** $t = 0.16$

(e) $t = 0.2$ **(f)** $t = 0.5$

Figure 9: Streamline normal stress for $\mu_f^s = 10^{-3}, \mu_c^s = 10^{-1}$ for $t = 0.04, \ldots, 0.2, 0.5$.

Fig. 10 illustrates some specific streamlines at times $t = 0.02, \ldots, 0.5$. The streamlines were chosen from the velocity field, during post-processing using Tecplot and are given in Fig. 10a. These streamlines were fixed and stepped through in time to produce the plots. Clearly, at $t = 0.04$, the bubble is collapsing spherically. At $t = 0.08$, not only can the remnants of bubble expansion be seen, but the tapering motion of the bubble is evident. This illustrates the Bjerknes-style attraction of the bubble towards the wall; the underside of the bubble will clearly migrate towards the rigid wall whilst the top of the bubble is still undergoing expansion due to its compressible contents. The attraction of the bubble towards the rigid wall, and hence the compression of the fluid layer, can be seen clearly at $t = 0.12$ with the layer response easily visible at $t = 0.16$. At later times $t = 0.2, 0.5$, the streamlines indicate that the bubble will migrate away from the rigid wall, but these are moments of temporary "repulsion" as the bubble centroid undergoes very low amplitude oscillations to and from the wall while settling to a steady state. Note that maximum velocity magnitude, across both components, is of the approximate order $10.0, 4.0$ and 1.0 for times $t = 0.04, 0.2$ and 0.5, respectively.

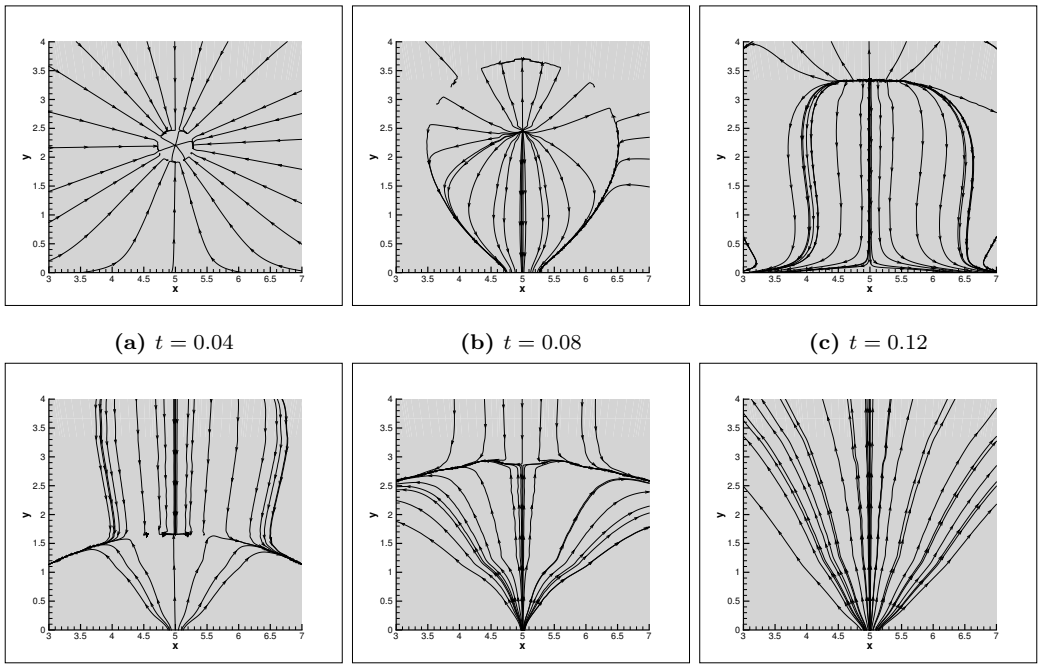

(a) $t = 0.04$ **(b)** $t = 0.08$ **(c)** $t = 0.12$

(d) $t = 0.16$ **(e)** $t = 0.2$ **(f)** $t = 0.5$

Figure 10: Velocity microstreams for selected streamlines for $\mu_f = 10^{-3}, \mu_c = 10^{-1}$ for $t = 0.04, \ldots, 0.2, 0.5$.

5.3. Ambient Fluid Viscosity greater than Fluid Layer Viscosity

In this section, we assume that the viscosity of the ambient fluid is greater than the viscosity of the fluid layer.

Fig. 11 illustrates the colour function at times $t = 0.2, 0.5, 10.0$ for material parameters $\mu_f =$

10^{-1} and $\mu_c = 10^{-3}$ (which are the opposite of the previous section). Plots of the colour function at times $t = 0.04, \ldots, 0.16$ have not been included as the motion of the bubble is remarkably similar to the previous section and therefore, the discussion for these times will not be repeated here. In the previous section, a near-steady state was attained (at $t \approx 0.2$) where only small oscillations and migrations of the bubble were seen, but surface perturbations were visible due to small viscosities. Here, however, the bubble shape remains smoother at $t = 0.2$ and $t = 0.5$ due to the larger ambient viscosity and consequently, as discussed in Section §5.1, the simulation is able to run for much longer times. Fig. 11c illustrates the colour function at the later time of $t = 10$. It is clear that the fluid-fluid interface is continuing to push upwards into the bubble after its rebound; after all it now has a lower viscosity and better retains its momentum, initially generated by the bubble collapse in the earlier stages. Brujan and co-workers [43] demonstrated that when a laser-generated cavitation bubble collapses near an elastic material (inertia dominated collapse), an ejection of the elastic material into the ambient fluid can be seen. A similar phenomenon is seen here, however due to the lower amount of inertia in these examples, the jet-like growth of the fluid-fluid interface does not pierce the bubble.

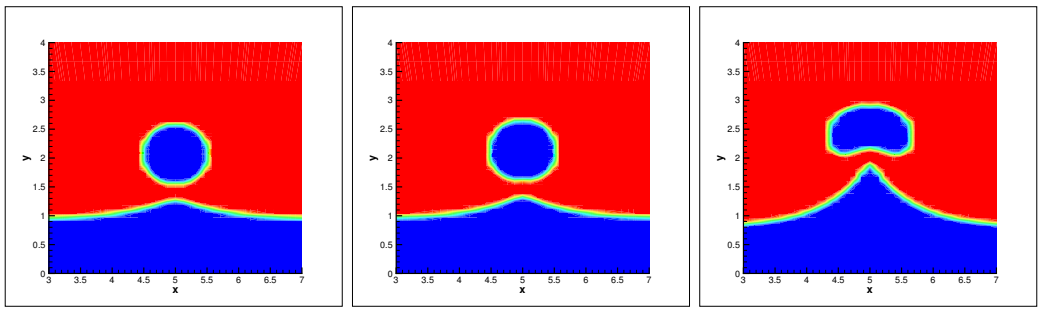

(a) $t = 0.2$ **(b)** $t = 0.5$ **(c)** $t = 10.0$

Figure 11: Colour function for $\mu_f = 10^{-1}, \mu_c = 10^{-3}$ for $t = 0.2, 0.5, 10$.

Fig. 12 illustrates contours of the streamline normal stress at times $t = 0.04, \ldots, 0.5$. At $t = 0.04$, a relatively large amount of normal stress appears radially around the bubble as it collapses. This normal stress clearly dissipates outwards at $t = 0.08$ during the bubble expansion phase. However, note that there is a build up of normal stress between the bubble and the layer which again may have implications for cavitation erosion. Also notice that, as the simulation progresses, the normal stresses then dissipate outwards and partly into the fluid layer while decreasing in magnitude. Figure 12g illustrates the normal stresses that are found at time $t = 10$. There is evidence of stress build-up on either side of the crest at the fluid-fluid interface. These stresses accompany the fluid mechanical motion that drives the interface upward. They are indicative of the retarding effect of the ambient fluid on the upwards jet, and also limit any possible penetration of the nearby bubble.

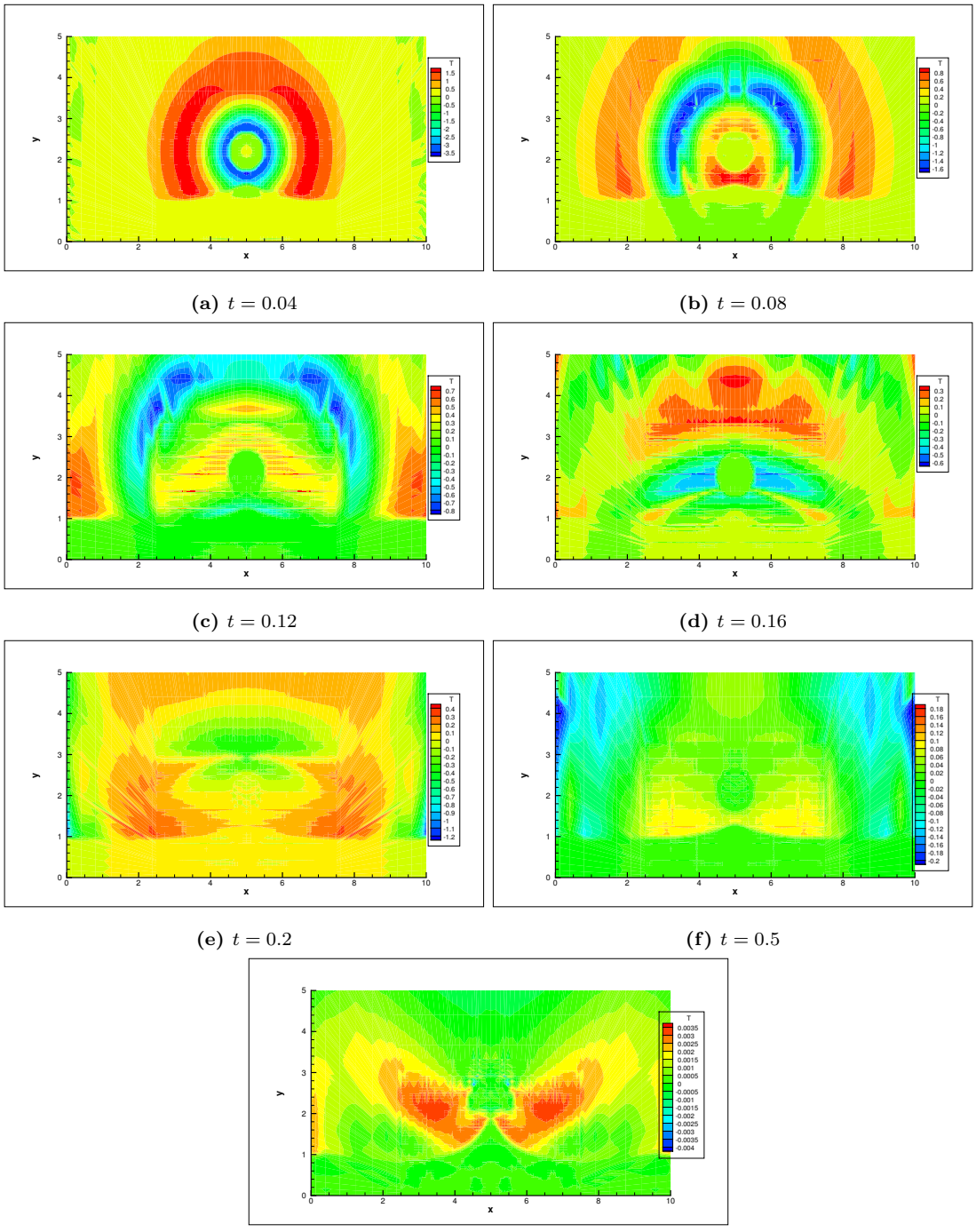

(a) $t = 0.04$ **(b)** $t = 0.08$

(c) $t = 0.12$ **(d)** $t = 0.16$

(e) $t = 0.2$ **(f)** $t = 0.5$

(g) $t = 10.0$

Figure 12: Streamline normal stress for $\mu_f = 10^{-1}, \mu_c = 10^{-3}$ for $t = 0.04, \ldots, 0.2, 0.5, 10$.

Similar to the previous section, Figs. 13a–13c illustrate a snapshot of specific streamlines at certain points in time. Plots of the streamlines at the earlier times of $t = 0.04, \ldots, 0.16$ have not been included as they are near identical to the previous section (see Figs. 10a–10d). Indeed, the similarity can still be seen in Figs. 13a and 13b. Therefore, the discussion will not be repeated

here. Fig. 13c illustrates the streamlines at $t = 10$. Immediately, one notices the presence of vortices inside the layer, created as fluid is drawn horizontally inward, then vertically upward to form the interface jet directed into the bubble.

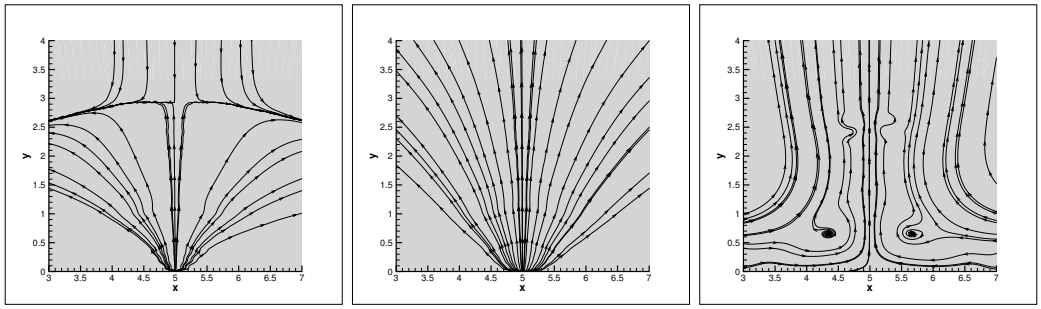

(a) $t = 0.2$ **(b)** $t = 0.5$ **(c)** $t = 10$

Figure 13: Velocity microstreams for selected streamlines for $\mu_f = 10^{-1}, \mu_c = 10^{-3}$ for $t = 0.2, 0.5, 10$.

It is expected that increasing the viscosity of the layer would decrease height of the fluid-fluid interface at $t = 10$. Indeed, this is illustrated in Fig. 14. As the dynamics are dominated by the pressure difference between the bubble and ambient fluid, the effect of varying viscosity is quite small, but still noticeable, with decreased deformation in both the interface and the bubble seen for $\mu_c = 10^{-1}$.

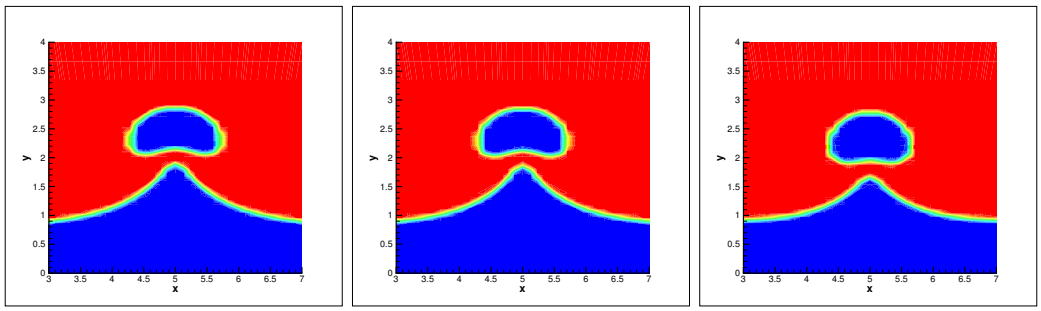

(a) $\mu_c = 10^{-3}$ **(b)** $\mu_c = 10^{-2}$ **(c)** $\mu_c = 10^{-1}$

Figure 14: Colour function for $\mu_c = 10^{-3}, 10^{-2}, 10^{-1}$, $\mu_f = 1.0$ when $t = 10$.

5.4. Fluid Layer Height Investigation

This section is concerned with a numerical study of the influence of the rigid wall which backs the fluid layer. Analogous to the previous section, the domain $\Omega = [0, 10] \times [0, 10]$ contains a gas-filled bubble, Ω_b, and a fluid layer, Ω_c, so that the ambient fluid occupies the domain $\Omega_f = \Omega \setminus (\Omega_b \cup \Omega_c)$. The bubble centre is positioned at $\bar{\boldsymbol{x}}$ (which varies depending on the layer height) with an initial radius $R = 1$. The bubbles contents are modelled as a compressible fluid with density $\rho_{b,0} = 0$ and a constant viscosity $\mu_b = 1 \times 10^{-5}$. The fluid layer occupies the domain $\Omega_c = [0, 10] \times [0, h]$ (where the height is given by $h = 0.3, 5.0$) and has the same density as the

ambient fluid, i.e. $\rho_{c,0} = \ln(4) = \rho_{f,0}$. The time step length is given by $\Delta t = 5 \times 10^{-3}$. Similarly to §4.3, we define three special marker particles which track the top and bottom of the bubble as well as the centre of the interface between the ambient fluid and the fluid layer. These marker particles are denoted by $\boldsymbol{x}_{top}$, $\boldsymbol{x}_{bot}$ and $\boldsymbol{x}_{int}$, respectively. We separate our results into two parts: when the ambient fluid viscosity is less than the layer viscosity and vice-versa.

5.4.1. Ambient fluid viscosity less than fluid layer viscosity

Throughout this subsection, we let $\mu_f = 10^{-3}$ and $\mu_c = 10^{-1}$. A comparison of the colour function, density and streamline normal stress for the two cell heights quoted above, is considered. The density is plotted in place of the fluid pressure, on the understanding that the two are equivalent to within a multiplicative constant through the linear equation of state (2). By choosing a small and a large fluid layer height, h, we can easily assess the influence of the rigid wall backing the layer.

Figure 15 illustrates a comparison of the colour function at interface heights $h = 0.3$ and 5.0. The plots are taken at time $t = 0.08$ as the majority of the dynamics occur early on the simulation. The difference in the bubble shape at the different heights is immediately obvious. At the smaller height, Fig. 15a, the bubble elongates towards the rigid wall (this behaviour was seen in the previous sections; see for example, Fig. 10b). Whilst at the larger height, Fig. 15b, the bubble remains approximately spherical. The reason for the substantial difference in bubble shapes can be immediately seen in the corresponding density contours illustrated in Fig. 16. Fig. 16a shows that there is a region of lower pressure on the rigid wall in the region directly beneath the bubble. Due to the absence of buoyancy and surface tension, the pressure gradient is the driving force for the bubble elongation and migration towards the wall. On the other hand, at a greater height, Fig. 16b shows that the region of low pressure is contained in an annulus around the bubble, which dissipates outwards as the simulation progresses; meanwhile the bubble continues near-spherical oscillations of decreasing amplitude. Clearly, the fluid layer thickness is sufficiently large so as to minimise any effect of the wall on the bubble.

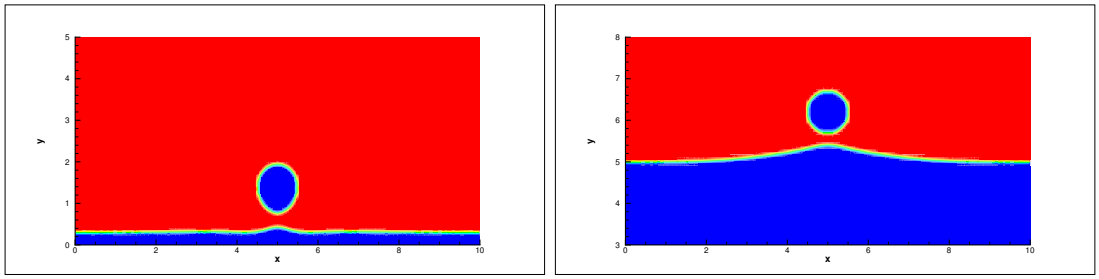

(a) $h = 0.3$ **(b)** $h = 5.0$

Figure 15: Colour function for $\mu_f = 10^{-3}, \mu_c = 10^{-1}$ at $t = 0.08$ with the fluid-fluid interface at heights $h = 0.3, 5.0$.

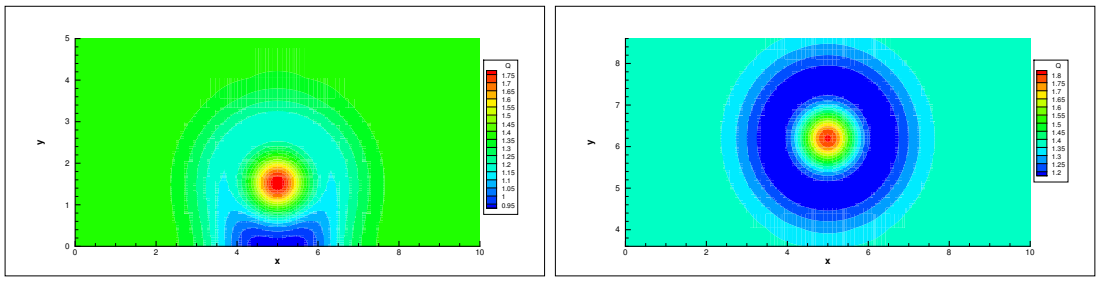

(a) $h = 0.3$ **(b)** $h = 5.0$

Figure 16: Density contour for $\mu_f = 10^{-3}, \mu_c = 10^{-1}$ at $t = 0.04$ with the fluid-fluid interface at heights $h = 0.3, 5.0$.

Figs. 17a and 17b illustrate the streamline normal stress at time $t = 0.08$ for heights $h = 0.3$ and 5.0, respectively. It is evident from Fig. 17a, that the normal stress is highest on the rigid wall, generated by the no-slip condition. This stress dissipates outwards along the rigid wall as the simulation progresses. For $h = 5.0$, Fig. 17b illustrates that the stress dissipates outwards in concentric circles in a manner similar to the density/pressure, but with notably larger magnitudes found within the fluid layer. This is expected as the fluid layer is of a larger viscosity (by some two orders of magnitude).

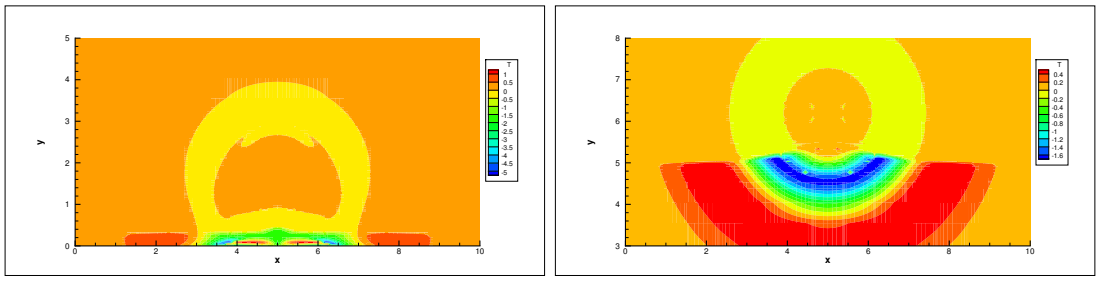

(a) $h = 0.3$ **(b)** $h = 5.0$

Figure 17: Streamline normal stress contour for $\mu_f = 10^{-3}, \mu_c = 10^{-1}$ at $t = 0.08$ with the fluid-fluid interface at heights $h = 0.3, 5.0$.

5.4.2. Ambient fluid viscosity greater than fluid layer viscosity

Following on from the previous subsection, we swap viscosities and let $\mu_f = 10^{-1}$ and $\mu_c = 10^{-3}$. It was illustrated in an earlier section, that the increased ambient fluid viscosity increases the lifetime of the bubble. Therefore, Figs. 18a and 18b illustrate the colour function at time $t = 10.0$ at interface heights 0.3 and 5.0, respectively. Immediately, one sees the effect the rigid wall has on the fluid-fluid interface and bubble shape. At a height of $h = 0.3$, a jet forms in the fluid-fluid interface which is more rounded and elongated than at a height of $h = 5.0$. The fluid-fluid interface, at $h = 0.3$, penetrates a little further into the bubble when compared to the $h = 0.5$ case, most likely due to the increased pressure build up (and subsequent rebound driving

force) in the smaller layer of fluid. Consequently, at the smaller height, the bubble can be seen to bend around the fluid-fluid interface much more significantly when compared to the larger height.

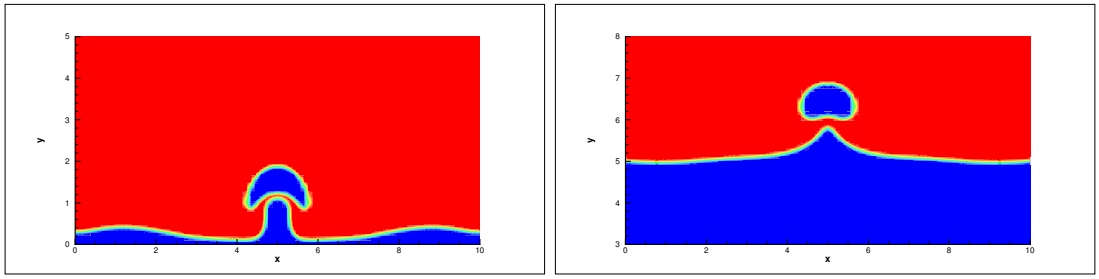

(a) $h = 0.3$ **(b)** $h = 5.0$

Figure 18: Colour function for $\mu_f = 10^{-1}, \mu_c = 10^{-3}$ at $t = 10.0$ with the fluid-cell interface at heights $h = 0.3, 5.0$.

In order to draw comparisons with the previous section, the streamline normal stress at time $t = 0.08$ is now considered. We do not consider comparisons for the colour function, density or microstreaming as results are found to be near-identical to the previous section for $t \leq 0.08$. Figs. 19a and 19b illustrate the streamline normal stress at interface heights 0.3 and 5.0, respectively, for time $t = 0.08$. Compared to the previous section, the largest build up stress is now seen in the ambient fluid. It is clear from Fig. 19a that there is a small build up of normal stress on the fluid-fluid interface which has possible implications for cell functionality, if the thin layer is representative of a thin cell layer. However, the same localised build-up is not clearly seen in Fig. 19b where the stress once again dissipates in concentric circles, but with magnitudes larger in the ambient fluid than the adjacent fluid layer. Note that we have not included plots of the normal stress contours at $t = 10$ because the stress is of negligible magnitude at this time for both heights.

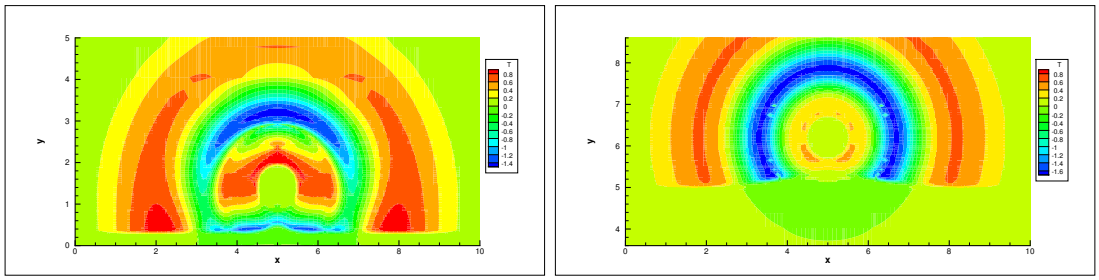

(a) $h = 0.3$ **(b)** $h = 5.0$

Figure 19: Streamline normal stress contour for $\mu_f = 10^{-1}, \mu_c = 10^{-3}$ at $t = 0.08$ with the fluid-cell interface at heights $h = 0.3, 5.0$.

6. Single Cell-Bubble Interaction for Sonoporation

One of the many applications of bubble dynamics is non-invasive and targeted drug delivery via sonoporation [4, 5, 6]. Drug-laden encapsulated microbubbles may be injected as a bubbly solution into the body, with ultrasound (applied at a desired location) acting to burst the bubbles and deliver the drug to the target site. Under the action of ultrasound, the bubble can collapse in two ways: so-called inertial (unstable) and non-inertial (stable) cavitation. The high speed liquid jet that tends to form in inertial cavitation may perforate the nearby cell (producing a pore in the cell membrane) and transport the drug into the cell through the perforation. It is not clear under what circumstances that the damage to the cell by the high speed liquid jet is usually repairable. Experiments by Hu *et al.* [44], show that if the jet produces a high amount of cell perforation with a large pore size, then the cell will not repair itself. In contrast, non-inertial cavitation can be sustained at lower ultrasound intensities, causing the bubble to oscillate but not burst or produce a high speed jet. At these lower intensities, several mechanisms have been proposed which may enable drug uptake into the cell [6]. It is possible that the oscillations of the bubble produce a pore in the cell membrane through the exertion of fluid mechanical stresses on the cell interface formed by the associated microstreaming flow [45]. It is also possible that the bubble would migrate into, or directly push upon, the nearby cell due to the acoustic forcing [6]. The above mechanical actions are in addition to biological processes where drug uptake may be achieved through endocytosis (the process by which cells absorb external molecules by engulfing them in their cell membrane). It is unknown which method produces the greater volume of drug delivery into the cell, but numerical simulations, such as those presented here, may offer important physical insights.

The results presented previously in this article, assume that the bubble is small in diameter in comparison to an adjacent fluid layer, which may model a large (locally flat) cell or a contaminant layer to be removed via microbubble cleaning. The diameter of cells in the human body can vary significantly, as can the diameter of microbubbles. For example, typically the diameter of an encapsulated microbubble used in conjunction with ultrasound, can vary between $1 - 10\ \mu m$ [46]. Therefore, this section presents the interaction between a bubble and a full suspended cell, where the two have similar spatial dimensions.

It was shown in the previous sections, that the interaction between the rigid wall and the bubble is dominant over the bubble-cell interaction. Therefore, our domain is chosen to be sufficiently large to negate any wall effects. Let $\Omega = [0, 20] \times [0, 20]$ and assume that the bubble is situated directly on top of the cell where the centre point between the cell and the bubble is placed in the centre of the domain. The initial configuration is illustrated in Fig. 20b and the associated mesh is depicted in Fig. 20a below. The mesh parameters are: $N = 10$, $\alpha_{max} = 12$, $\beta_{max} = 12$.

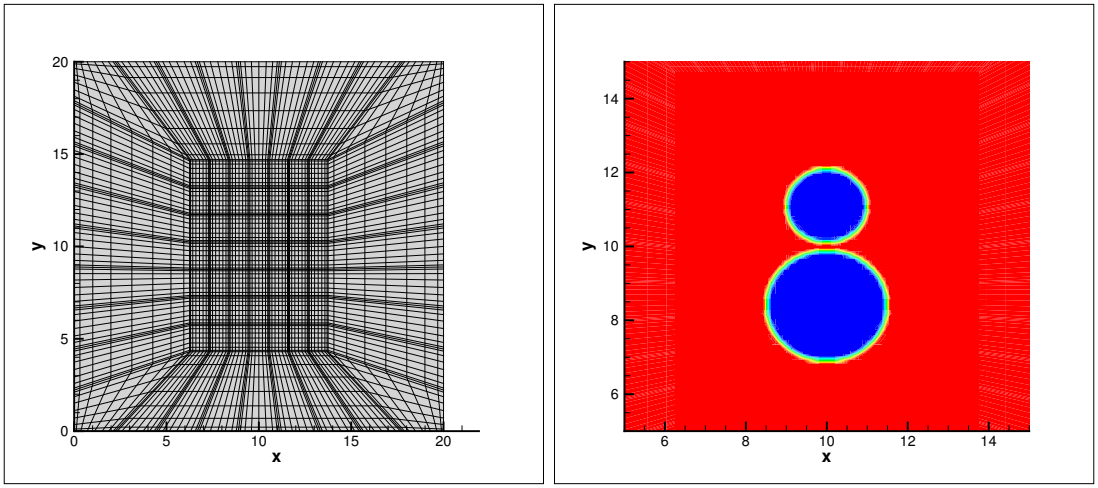

(a) Example of Mesh 3 with $N = \alpha_{max} = \beta_{max} = 8$; refined region is a box containing both the bubble and the cell

(b) Initial configuration

The dimensional and non-dimensional parameters used in this section are given in Table 2. To calculate the non-dimensional parameters, we employ the same scaling as given earlier in §2.1 where the initial bubble radius $R = 1\ \mu m$, initial bubble density $\rho_{b,0} = 1\ kg{\cdot}m^{-3}$ and the reference speed of sound $V = 3 \times 10^2\ ms^{-1}$ (the speed of sound through the air phase). The bubble, fluid and cell viscosities are of the (approximate) orders typically found for air, blood plasma and a red blood cell's haemoglobin solution (see e.g. [47]), respectively.

		Dimensional	Non-Dimensional
Radius	Bubble	$R_{b,0} = 10^{-6}$	$R^*_{b,0} = 1$
	Cell	$R_{c,0} = 1.5 \times 10^{-6}$	$R^*_{c,0} = 1.5$
Density	Bubble	$\rho_{b,0} = 1$	$\rho^*_{b,0} = 1$
	Fluid	$\rho_{f,0} = 0.2$	$\rho^*_{f,0} = 0.2$
	Cell	$\rho_{c,0} = 0.2$	$\rho^*_{c,0} = 0.2$
Dynamic Viscosity	Bubble	$\eta_{b,0} = 10^{-5}$	$\eta^*_{b,0} = 0.033$
	Fluid	$\eta_{f,0} = 10^{-4}$	$\eta^*_{f,0} = 0.333$
	Cell	$\eta_{c,0} = 10^{-3}$	$\eta^*_{c,0} = 3.333$
Kinematic Viscosity	Bubble	$\mu_{b,0} = 10^{-5}$	$\mu^*_{b,0} = 0.033$
	Fluid	$\mu_{f,0} = 5 \times 10^{-4}$	$\mu^*_{f,0} = 1.665$
	Cell	$\mu_{c,0} = 5 \times 10^{-3}$	$\mu^*_{c,0} = 16.665$
Speed of Sound		$c_0 = 1500$	$c^*_0 = 5$

Table 2: Dimensional and non-dimensional parameters used in this section.

Figure 21 illustrates the colour function at times $t = 0.1, 0.2, 0.3, 0.5$. In contrast to the previous sections, the initial density (and therefore, initial pressure) inside the bubble is taken to be larger than the density in the ambient fluid and therefore, the bubble goes through an expansion phase initially (i.e. the bubble response in an ultrasound wave trough). As the bubble expands, it pushes into the nearby cell which causes a flattening of both the cell and the bubble, which can clearly be seen in Figs. 21b-21d. At later times, the gap between the bubble and cell increases slightly due to the continuing expansion of the bubble pushing the cell downwards.

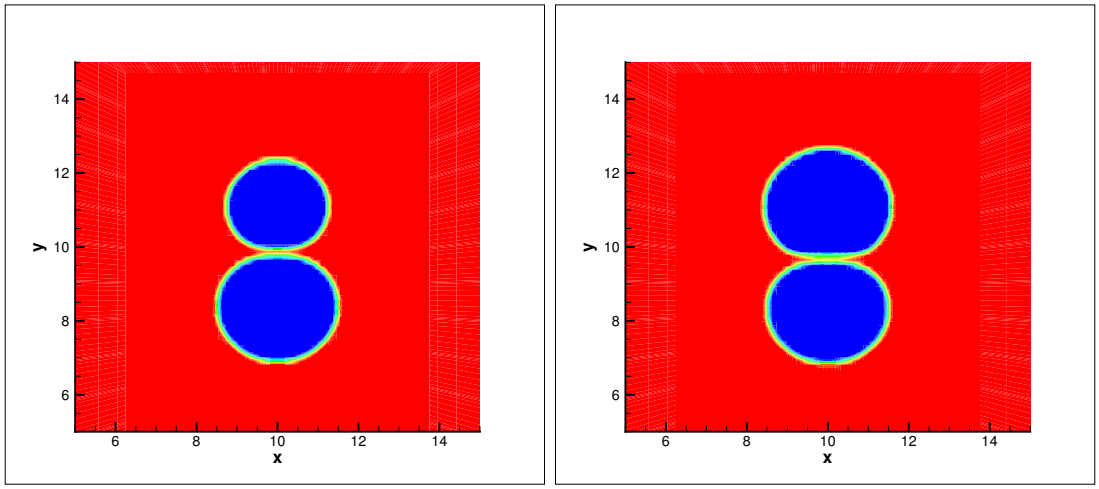

(a) $t = 0.1$ **(b)** $t = 0.2$

(c) $t = 0.3$ **(d)** $t = 0.5$

Figure 21: Colour function at times $t = 0.0, 0.1, 0.2, 0.3, 0.5, 1.0$.

Figure 22 illustrates the density contours at time levels $t = 0.1, 0.2, 0.3, 0.5$. It can be clearly seen in Fig. 22a that a pressure wave is released approximately spherically, into the surrounding fluid and dissipates fairly rapidly. At later times, Figs. 22b and 22c illustrate that a region of high pressure develops, and persists, at the bottom of the bubble (and top of cell surface) as a result

of the bubble expansion into the cell.

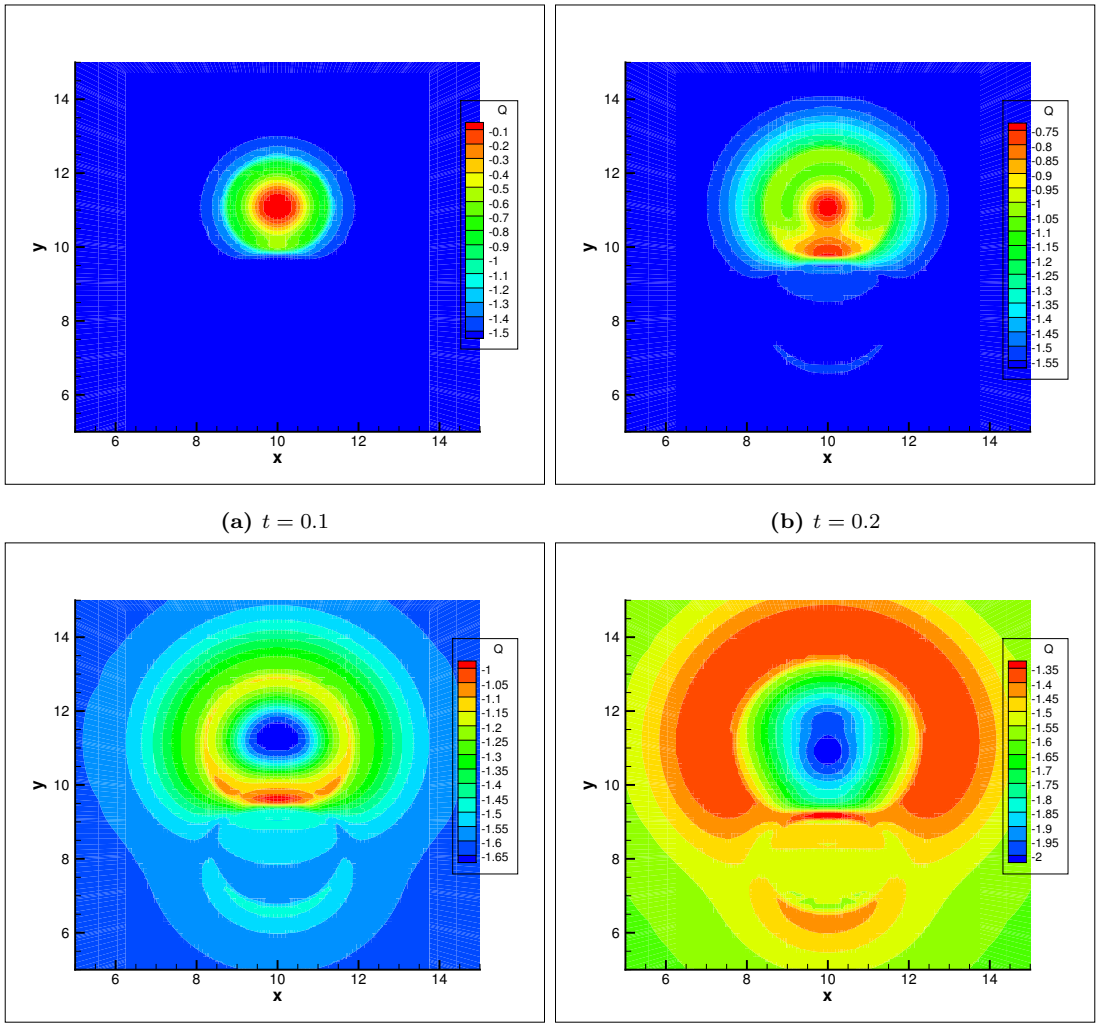

(a) $t = 0.1$ **(b)** $t = 0.2$

(c) $t = 0.3$ **(d)** $t = 0.5$

Figure 22: Density contour at times $t = 0.0, 0.1, 0.2, 0.3, 0.5$.

Figure 23 illustrates the streamline normal stress contour at time levels $t = 0.1, 0.2, 0.3, 0.5$. Notice that the location of highest normal stress magnitude is at the top of the cell. This high normal stress region at the cell interface is sustained for the whole simulation, even as the normal stress elsewhere begins to spread and dissipate around the cell surface. Due to the normal stress being concentrated at a specific location in the cell, it could have potentially negative implications for cell functionality.

It is well known that during stable cavitation the oscillations of the bubble induce so-called microstreaming local to the bubble (see e.g. [6, 45]). This microstreaming produces a shear stress (as well as a normal stress) on the membrane of the cell. Figure 24 illustrates the build up of streamline shear stress on the fluid-cell interface. Figure 24c illustrates that the shear stress

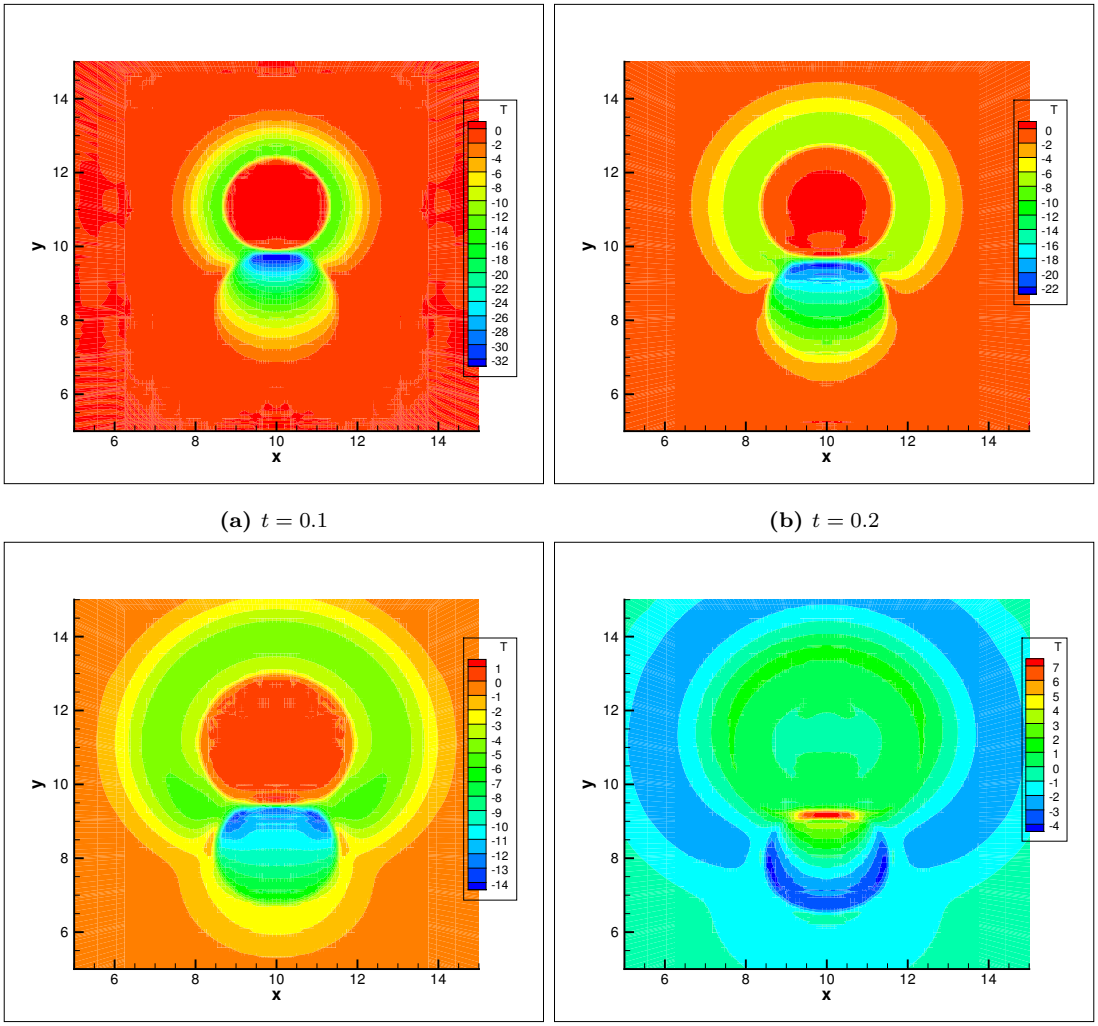

(a) $t = 0.1$ **(b)** $t = 0.2$

(c) $t = 0.3$ **(d)** $t = 0.5$

Figure 23: Streamline normal stress contour at times $t = 0.1, 0.2, 0.3, 0.5$.

spreads around the fluid-cell interface from towards the top of the cell to the middle, implying that a cavitating bubble can have a global effect on the cell. Leow *et al.* [48], showed that so-called *blebbing* (a term used to describe a local distortions in the membrane of a cell) occurred, not only at the sonoporation site (e.g. the site of jet impact - inertial cavitation) but also along the membrane periphery. It was concluded that blebbing at the impact site may be involved in the cell's repair process but no reasons are offered for the additional blebbing found along the membranes periphery. Leow *et al.* [48] do indicate that non-local blebbing is quite likely, given that the actin cytoskeleton (a fibrous network in the interior of a cell which is connected to the cell membrane) is disrupted (see e.g. [49]). The results presented here illustrate spreading of both the normal and shear stresses along the cell membrane: a phenomenon purely hydrodynamical in nature. This raises the possibility that the hydrodynamical spreading of normal and shear stresses

is the key mechanism in creating non-localised blebbing (and also non-local disruption of the actin cytoskeleton close to the cell membrane), rather than any biochemical cell response.

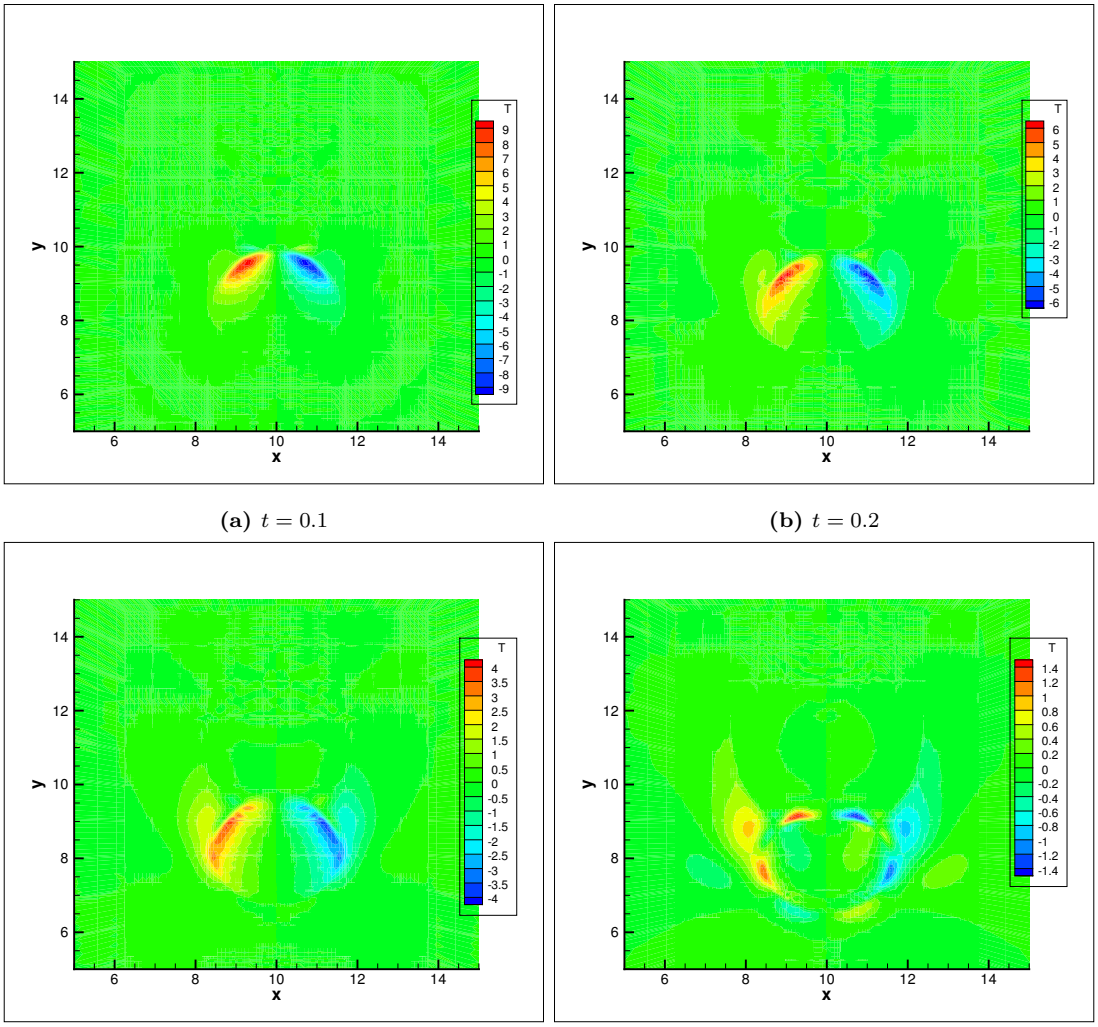

(a) $t = 0.1$ **(b)** $t = 0.2$

(c) $t = 0.3$ **(d)** $t = 0.5$

Figure 24: Streamline shear stress contour at times $t = 0.1, 0.2, 0.3, 0.5$.

7. Conclusions and Future Work

In this article, we have extended the spectral element marker particle (SEMP) method to incorporate a third-phase. The full compressible, two-dimensional governing equations are solved using the spectral element method, whilst the three fluid phases are tracked using the marker particle method - a scheme that bears a strong resemblence to VOF methods. The marker particle method was validated using a time-reversed rotation, where it was evident that the method exhibited approximately linear convergence with respect to increasing marker particle density. A satisfactory result given the highly complex three-phase distortion observed. The SEMP method was then

validated on two examples: a three-phase steady-state Poiseuille flow example (the analytical solution is derived in the Appendix A) and bubble collapse near a highly viscous fluid-layer (which approximates a rigid wall). For the Poiseuille flow example, good qualitative agreement could be seen between the analytical and computed velocity solutions. However, the v component of the velocity field contained non-zero components which were attributed to an unavoidable smoothing error, present due to the continuous (smoothed) material parameters across the fluid-fluid interfaces. Nevertheless, a reasonable value of the maximum norm error between the analytical and computed velocity was given after long simulation times. The three-phase bubble collapse near a highly viscous fluid-layer gave good qualitative agreement with the two-phase bubble collapse near a rigid wall case presented by Lind and Phillips [26].

A numerical investigation of low-inertia bubble collapse backed by a rigid wall was then presented. It was illustrated that SEMP exhibited mesh independence (under p-refinement) for reasonable time-scales ($O(1)$ time units). A numerical study of the influence of viscosity was then undertaken, with various values and combinations considered, including cases when the ambient fluid viscosity is greater than the fluid layer, and vice versa. When the ambient fluid viscosity is less than the fluid layer viscosity, a localised peak normal stress was seen in the central bump of the fluid-fluid interface. The fact that the normal stress is localised has potential implications for cell functionality. When the ambient fluid viscosity is greater than the fluid layer viscosity, the simulation remained stable for larger computational times. At larger times, the fluid layer continued pushing upwards into the bubble as a result of better momentum retention in the layer. At these later times, there was evidence of stress build up on either side of the crest of the fluid-fluid interface. These stresses are indicative of a retarding effect of the ambient fluid on the upwards motion of the fluid-fluid interface. Voritces were shown to be present in the fluid layer at these later times. An investigation of the height between the fluid-fluid interface and the rigid wall which backs the fluid-cell was then presented. It was shown that the bubble collapsed spherically at greater interface heights from the rigid wall as result of the reduced interaction between the bubble and the rigid wall.

Finally, a bioengineering example was considered. A bubble was placed near a fluid-cell with material parameters typical of air, blood plasma and a red blood cell haemoglobin solution. A region of high pressure developed at the cell surface as a result of the interaction between the cell and bubble, and this persisted for the duration of the simulation. Initially, a high amount of normal stress was seen to build up at the top of the cell and this then spread out along the cell interface. Similar behaviour was also seen for the shear stress where the shear stress is caused by the bending of velocity streamlines around the cell. The fact that the normal and shear stresses spread out along the cell interface is a potential reason for the non-localised blebbing phenomenon seen as a cell membrane recovers post bubble/ultrasound interaction [48]. We stress that all of

the phenomena quoted above are purely hydrodynamical and are solely caused by the interaction between the fluid cell and the oscillating bubble.

Acknowledgements

Support from the Engineering and Physical Sciences Research Council of the United Kingdom, grant no. EP/L011549/1, is gratefully acknowledged. All of this work was performed using the computational facilities of the Computationally-Intensive Research (CIR) ecosystem at the University of Manchester. The data used in this article is freely and openly available `https://dx.doi.org/10.6084/m9.figshare.3100129`.

Appendix A. Analytical Solution for Three-Phase Steady-State Poiseuille Flow

In this appendix, we derive the analytical solution for steady-state Poiseuille flow of three adjacent immiscible fluids. This derivation follows the solution of Bird *et al.* [42] for two-phase Poiseuille flow. As mentioned earlier, consider three immiscible, incompressible fluids flowing in the x direction in a horizontal thin slit of length L and height H under the influence of a horizontal pressure gradient $\partial p/\partial x = P$. Thus, we define our domain $\Omega = [0, L] \times [0, H]$, which contains three distinct phases: $\Omega_1 = [0, L] \times [0, a]$, $\Omega_2 = [0, L] \times [a, b]$ and $\Omega_3 = [0, L] \times [b, H]$. The liquid phases are flowing sufficiently slowly so that the fluid-fluid interfaces remain planar. Note that the fluids in each phase have distinct viscosities, η_1, η_2 and η_3.

The equations governing incompressible fluid motion are given by

$$\rho \frac{D\boldsymbol{u}}{Dt} = -\nabla p + \nabla \cdot \boldsymbol{S}, \tag{A.1a}$$

$$\nabla \cdot \boldsymbol{u} = 0, \tag{A.1b}$$

$$\boldsymbol{S} = \eta(\nabla \boldsymbol{u} + \nabla \boldsymbol{u}^T), \tag{A.1c}$$

where ρ is the constant density, η is the constant viscosity, $\boldsymbol{u}$ is the velocity, p is the pressure and $\boldsymbol{S}$ is the extra-stress tensor. In addition to the constant pressure gradient in the x direction, steady-state Poiseuille flow assumes that the pressure is a function of x alone, $p = p(x)$, that the velocity field has the form $\boldsymbol{u} = (u, v) = (u(y), 0)$ and that there is no time-dependence $\partial/\partial t = 0$. Thus, in component form, Eqn. (A.1a) reduces to

$$0 = -P + \frac{\partial S_{xx}}{\partial x} + \frac{\partial S_{xy}}{\partial y}, \tag{A.2a}$$

$$0 = \frac{\partial S_{xy}}{\partial x} + \frac{\partial S_{yy}}{\partial y} \tag{A.2b}$$

Note that the incompressible constraint (A.1b) is automatically satisfied by the assumption on the velocity field. The components of the extra-stress tensor (Eqn. (A.1c)) are given by

$$S_{xx} = 0, \qquad S_{xy} = \eta \frac{\partial u}{\partial y} = S_{yx}, \qquad S_{yy} = 0 \tag{A.3}$$

Substituting the extra-stress components (Eqn. (A.3)) into Eqn. (A.2) causes the y component of the momentum equation (Eqn. (A.2b)) to vanish and the x component (Eqn. (A.2a)) reduces to

$$\frac{\partial S_{xy}}{\partial y} = P \tag{A.4}$$

Equation (A.4) holds for each phase $i = 1, 2, 3$. Thus, integrating Eqn. (A.4) with respect to y yields

$$S^i_{xy} = Py + C^i_1, \tag{A.5}$$

where $i = 1, 2, 3$ denotes each fluid phase and the arbitrary coefficients of integration C^i_1 are constant because S^i_{xy} has no dependence on x. According to Bird *et al.* [42], the shear stress must be continuous across each fluid-fluid interface. Thus, we have two boundary conditions on the shear stress

$$S^1_{xy} = S^2_{xy} \qquad \text{when } y = a, \tag{A.6a}$$

$$S^2_{xy} = S^3_{xy} \qquad \text{when } y = b, \tag{A.6b}$$

where $y = a$ and $y = b$ denote the interfaces between the fluid phases. Applying the boundary conditions (A.6) to the shear stress (Eqn. (A.5)) for each phase tells us that $C^1_1 = C^2_1 = C^3_1 = C_1$. Using the definition of the shear stress, Eqn. (A.5) becomes

$$\frac{\partial u_i}{\partial y} = \frac{P}{\eta_i} y + \frac{C_1}{\eta_i}, \tag{A.7}$$

where u_i denotes the x component of the velocity field for fluid i and η_i is the viscosity of fluid i, $i = 1, 2, 3$. Integrating Eqn. (A.7) throughout with respect to y yields

$$u_i = \frac{P}{2\eta_i} y^2 + \frac{C_1}{\eta_i} y + C^i_2, \tag{A.8}$$

for each fluid phase i. We have four coefficients which need to be determined; fortunately, we have four boundary conditions on the velocity:

$$u_1 = 0 \qquad \text{when } y = 0, \tag{A.9a}$$

$$u_1 = u_2 \qquad \text{when } y = a, \tag{A.9b}$$

$$u_2 = u_3 \qquad \text{when } y = b, \tag{A.9c}$$

$$u_3 = 0 \qquad \text{when } y = H \tag{A.9d}$$

Applying Eqn. (A.9a) to Eqn. (A.8) with $i = 1$ tells us that $C^1_2 = 0$. Similarly, applying the other boundary conditions on the velocity to Eqn. (A.8) for each phase i yields

$$\frac{Pa^2}{2\eta_1} + \frac{C^1 a}{\eta_1} = \frac{Pa^2}{2\eta_2} + \frac{C^1 a}{\eta_2} + C^2_2, \tag{A.10a}$$

$$\frac{Pb^2}{2\eta_2} + \frac{C^1 b}{\eta_2} + C^2_2 = \frac{Pb^2}{2\eta_3} + \frac{C^1 b}{\eta_3} + C^3_2, \tag{A.10b}$$

$$\frac{PH^2}{2\eta_3} + \frac{C^1 H}{\eta_3} + C^3_2 = 0 \tag{A.10c}$$

Immediately, it can be seen that Eqns. (A.10a) and (A.10c) can be rearranged to write C_2^2 and C_2^3 in terms of C^1. Substituting these into Eqn. (A.10b) yields an expression for C_1. Once C_1 is known, then C_2^2 and C_2^3 can be determined from Eqns. (A.10a) and (A.10c). Therefore, the three-phase steady-state Poiseuille flow solution is given by

$$C^1 = \frac{\left[\frac{Pa^2}{2\eta_1} + \frac{P}{2\eta_2}(b^2 - a^2) + \frac{P}{2\eta_3}(H^2 - b^2)\right]}{\left[\frac{1}{\eta_2}(a-b) + \frac{1}{\eta_3}(b-H) - \frac{a}{\eta_1}\right]}, \tag{A.11a}$$

$$C_2^2 = \frac{Pa^2}{2\eta_1} + \frac{C^1 a}{\eta_1} - \frac{Pa^2}{2\eta_2} - \frac{C^1 a}{\eta_2}, \tag{A.11b}$$

$$C_2^3 = -\frac{PH^2}{2\eta_3} - \frac{C^1 H}{\eta_3}, \tag{A.11c}$$

$$u_1(y) = \frac{P}{2\eta_1}y^2 + \frac{C_1}{\eta_1}y + C_2^1, \tag{A.11d}$$

$$u_2(y) = \frac{P}{2\eta_2}y^2 + \frac{C_1}{\eta_2}y + C_2^2, \tag{A.11e}$$

$$u_3(y) = \frac{P}{2\eta_3}y^2 + \frac{C_1}{\eta_3}y + C_2^3 \tag{A.11f}$$

It is straightforward to show that the analytical solution given in Eqn. (A.11) remains valid for the log density formulation used in this article.

[1] Lord Rayleigh O.M. F.R.S., VIII. on the pressure developed in a liquid during the collapse of a spherical cavity, Philosophical Magazine Series 6 34 (200) (1917) 94–98. doi:10.1080/14786440808635681.

[2] T. B. Benjamin, A. T. Ellis, The collapse of cavitation bubbles and the pressures thereby produced against solid boundaries, Philosophical Transactions of the Royal Society of London A: Mathematical, Physical and Engineering Sciences 260 (1110) (1966) 221–240. doi:10.1098/rsta.1966.0046.

[3] W. Lauterborn, C.-D. Ohl, Cavitation bubble dynamics, Ultrasonics Sonochemistry 4 (2) (1997) 65–75. doi:10.1016/S1350-4177(97)00009-6.

[4] J. Wu, W. L. Nyborg, Ultrasound, cavitation bubbles and their interaction with cells, Advanced Drug Delivery Reviews 60 (10) (2008) 1103–1116. doi:10.1016/j.addr.2008.03.009.

[5] S. Hernot, A. L. Klibanov, Microbubbles in ultrasound-triggered drug and gene delivery, Advanced Drug Delivery Reviews 60 (10) (2008) 1153–1166. doi:10.1016/j.addr.2008.03.005.

[6] I. Lentacker, I. D. Cock, R. Deckers, S. D. Smedt, C. Moonen, Understanding ultrasound induced sonoporation: Definitions and underlying mechanisms, Advanced Drug Delivery Reviews 72 (2014) 49–64. doi:10.1016/j.addr.2013.11.008.

[7] T. Kodama, K. Takayama, Dynamic behavior of bubbles during extracorporeal shock-wave lithotripsy, Ultrasound in Medicine & Biology 24 (5) (1998) 723–738. doi:10.1016/S0301-5629(98)00022-2.

[8] J. B. Freund, R. K. Shukla, A. P. Evan, Shock-induced bubble jetting into a viscous fluid with application to tissue injury in shock-wave lithotripsy, The Journal of the Acoustical Society of America 126 (5) (2009) 2746–2756. doi:10.1121/1.3224830.

[9] E. C. Unger, T. O. Matsunaga, T. McCreery, P. Schumann, R. Sweitzer, R. Quigley, Therapeutic applications of microbubbles, European Journal of Radiology 42 (2) (2002) 160–168. doi:10.1016/S0720-048X(01)00455-7.

[10] C.-Y. Ting, C.-H. Fan, H.-L. Liu, C.-Y. Huang, H.-Y. Hsieh, T.-C. Yen, K.-C. Wei, C.-K. Yeh, Concurrent blood-brain barrier opening and local drug delivery using drug-carrying microbubbles and focused ultrasound for brain glioma treatment, Biomaterials 33 (2) (2012) 704–712. doi:10.1016/j.biomaterials.2011.09.096.

[11] W. D. Song, M. H. Hong, B. Lukyanchuk, T. C. Chong, Laser-induced cavitation bubbles for cleaning of solid surfaces, Journal of Applied Physics 95 (6) (2004) 2952–2956. doi:10.1063/1.1650531.

[12] G. L. Chahine, A. Kapahi, J.-K. Choi, C.-T. Hsiao, Modeling of surface cleaning by cavitation bubble dynamics and collapse, Ultrasonics Sonochemistry 29 (2016) 528–549. doi:10.1016/j.ultsonch.2015.04.026.

[13] J. R. Blake, B. B. Taib, G. Doherty, Transient cavities near boundaries. Part 1. Rigid boundary, Journal of Fluid Mechanics 170 (1986) 479–497. doi:10.1017/S0022112086000988.

[14] J. R. Blake, B. B. Taib, G. Doherty, Transient cavities near boundaries. Part 2. Free surface, Journal of Fluid Mechanics 181 (1987) 197–212. doi:10.1017/S0022112087002052.

[15] E. Klaseboer, B. C. Khoo, Boundary integral equations as applied to an oscillating bubble near a fluid-fluid interface, Computational Mechanics 33 (2) (2004) 129–138. doi:10.1007/s00466-003-0508-2.

[16] E. Klaseboer, B. C. Khoo, An oscillating bubble near an elastic material, Journal of Applied Physics 96 (10) (2004) 5808–5818. doi:10.1063/1.1803925.

[17] G. A. Curtiss, D. M. Leppinen, Q. X. Wang, J. R. Blake, Ultrasonic cavitation near a tissue layer, Journal of Fluid Mechanics 730 (2013) 245–272. doi:10.1017/jfm.2013.341.

[18] Q. X. Wang, J. R. Blake, Non-spherical bubble dynamics in a compressible liquid. Part 1. Travelling acoustic wave, Journal of Fluid Mechanics 659 (2010) 191–224. doi:10.1017/S0022112010002430.

[19] Q. Wang, Multi-oscillations of a bubble in a compressible liquid near a rigid boundary, Journal of Fluid Mechanics 745 (2014) 509–536. doi:10.1017/jfm.2014.105.

[20] P. J. Shopov, P. D. Minev, I. B. Bazhlekov, Z. D. Zapryanov, Interaction of a deformable bubble with a rigid wall at moderate reynolds numbers, Journal of Fluid Mechanics 219 (1990) 241–271. doi:10.1017/S0022112090002932.

[21] P. J. Shopov, P. D. Minev, The unsteady motion of a bubble or drop towards a liquid-liquid interface, Journal of Fluid Mechanics 235 (1992) 123–141. doi:10.1017/S002211209200106X.

[22] P. J. Shopov, P. D. Minev, I. B. Bazhlekov, Numerical method for unsteady viscous hydrodynamical problem with free boundaries, International Journal for Numerical Methods in Fluids 14 (6) (1992) 681–705. doi:10.1002/fld.1650140604.

[23] S. Popinet, S. Zaleski, Bubble collapse near a solid boundary: a numerical study of the influence of viscosity, Journal of Fluid Mechanics 464 (2002) 137–163. doi:10.1017/S002211200200856X.

[24] M. Lee, E. Klaseboer, B. C. Khoo, On the boundary integral method for the rebounding bubble, Journal of Fluid Mechanics 570 (2007) 407–429. doi:10.1017/S0022112006003296.

[25] S. Müller, P. Helluy, J. Ballmann, Numerical simulation of a single bubble by compressible two-phase fluids, International Journal for Numerical Methods in Fluids 62 (6) (2010) 591–631. doi:10.1002/fld.2033.

[26] S. Lind, T. N. Phillips, Bubble collapse in compressible fluids using a spectral element marker particle method. Part 1. Newtonian fluids, International Journal for Numerical Methods in Fluids 70 (9) (2012) 1167–1187. doi:10.1002/fld.2737.

[27] S. J. Lind, T. N. Phillips, Bubble collapse in compressible fluids using a spectral element marker particle method. Part 2. Viscoelastic fluids, International Journal for Numerical Methods in Fluids 71 (9) (2013) 1103–1130. doi:10.1002/fld.3701.

[28] W. J. Rider, D. B. Kothe, A marker particle method for interface tracking, in: H. A. Dwyer (Ed.), Proceedings of the Sixth International Symposium on Computational Dynamics, Davis, CA, 1995, pp. 976–981.

[29] C. Hirt, B. Nichols, Volume of fluid (vof) method for the dynamics of free boundaries, Journal of Computational Physics 39 (1) (1981) 201–225. doi:10.1016/0021-9991(81)90145-5.

[30] F. H. Harlow, J. E. Welch, Numerical calculation of timedependent viscous incompressible flow of fluid with free surface, Physics of Fluids 8 (12) (1965) 2182–2189. doi:10.1063/1.1761178.

[31] S. W. Ohl, E. Klaseboer, B. C. Khoo, The dynamics of a non-equilibrium bubble near biomaterials, Physics in Medicine and Biology 54 (20) (2009) 6313.
URL http://stacks.iop.org/0031-9155/54/i=20/a=019

[32] M. Gad-el-Hak, Questions in Fluid Mechanics: Stokes' Hypothesis for a Newtonian, Isotropic Fluid., ASME. Journal of Fluids Engineering 117 (1) (1995) 3–5. doi:10.1115/1.2816816.

[33] P. C. Bollada, T. N. Phillips, On the effects of a compressible viscous lubricant on the load-bearing capacity of a journal bearing, International Journal for Numerical Methods in Fluids 55 (11) (2007) 1091–1120. doi:10.1002/fld.1545.

[34] P. C. Bollada, T. N. Phillips, An anisothermal, compressible, piezoviscous model for journal-bearing lubrication, International Journal for Numerical Methods in Fluids 58 (1) (2008) 27–55. doi:10.1002/fld.1705.

[35] A. T. Patera, A spectral element method for fluid dynamics: Laminar flow in a channel expansion, Journal of Computational Physics 54 (3) (1984) 468–488. doi:10.1016/0021-9991(84)90128-1.

[36] R. A. Adams, J. J. F. Fournier, Sobolev Spaces, Pure and Applied Mathematics, Academic Press, 2003.

[37] C. R. Schneidesch, M. O. Deville, Chebyshev collocation method and multi-domain decomposition for navier-stokes equations in complex curved geometries, Journal of Computational Physics 106 (2) (1993) 234–257. doi:10.1016/S0021-9991(83)71105-8.

[38] G. E. Karniadakis, S. Sherwin, Spectral/hp Element Methods for Computational Fluid Dynamics. 2nd Ed., Numerical Mathematics and Scientific Computation, Oxford University Press, 2005. doi:10.1093/acprof:oso/9780198528692.001.0001.

[39] R. G. Owens, T. N. Phillips, Computational Rheology, Imperial College Press, 2002.

[40] F. Bierbrauer, S.-P. Zhu, A numerical model for multiphase flow based on the GMPPS formulation. Part I: Kinematics, Computers & Fluids 36 (7) (2007) 1199–1212. doi:10.1016/j.compfluid.2006.12.001.

[41] F. Bierbrauer, T. N. Phillips, The numerical prediction of droplet deformation and break-up using the Godunov marker-particle projection scheme, International Journal for Numerical Methods in Fluids 56 (8) (2008) 1155–1160. doi:10.1002/fld.1710.

[42] R. B. Bird, W. E. Stewart, E. N. Lightfoot, Transport Phenomena. 2nd ed., John Wiley & Sons, Inc, 2007.

[43] E.-A. Brujan, K. Nahen, P. Schmidt, A. Vogel, Dynamics of laser-induced cavitation bubbles near an elastic boundary, Journal of Fluid Mechanics 433 (2001) 251–281. doi:10.1017/S0022112000003347.

[44] Y. Hu, J. M. F. Wan, A. C. H. Yu, Membrane perforation and recovery dynamics in microbubble-mediated sonoporation, Ultrasound in Medicine & Biology 39 (12) (2013) 2393–2405. doi:10.1016/j.ultrasmedbio.2013.08.003.

[45] J. Wu, Theoretical study on shear stress generated by microstreaming surrounding contrast agents attached to living cells, Ultrasound in Medicine & Biology 28 (1) (2002) 125–129. doi:10.1016/S0301-5629(01)00497-5.

[46] I. D. Cock, E. Zagato, K. Braeckmans, Y. Luan, N. de Jong, S. C. D. Smedt, I. Lentacker, Ultrasound and microbubble mediated drug delivery: Acoustic pressure as determinant for uptake via membrane pores or endocytosis, Journal of Controlled Release 197 (2015) 20–28. doi:http://dx.doi.org/10.1016/j.jconrel.2014.10.031.

[47] B. L. McClain, I. J. Finkelstein, M. D. Fayer, Dynamics of Hemoglobin in Human Erythrocytes and in Solution: Influence of Viscosity Studied by Ultrafast Vibrational Echo Experiments, Journal of the American Chemical Society 126 (48) (2004) 15702–15710. doi:10.1021/ja0454790.

[48] R. S. Leow, J. M. F. Wan, A. C. H. Yu, Membrane blebbing as a recovery manoeuvre in site-specific sonoporation mediated by targeted microbubbles, Journal of The Royal Society Interface 12 (105) (2015) 20150029. doi:10.1098/rsif.2015.0029.

[49] X. Chen, R. S. Leow, Y. Hu, J. M. F. Wan, A. C. H. Yu, Single-site sonoporation disrupts actin cytoskeleton organization, Journal of The Royal Society Interface 11 (95). doi:10.1098/rsif.2014.0071.

School of Mechanical, Aerospace and Civil Engineering,
The University of Manchester,
Manchester,
M13 9PL, UK.

4th April 2016

Dear Editor,

Please find attached the manuscript:

Bubble Collapse near a Fluid-Fluid Interface using the Spectral Element Marker Particle Method with Applications in Bioengineering

co-authored with Dr. Steven Lind, submitted for publication in the International Journal of Multiphase Flow.

This paper presents the application of the spectral element marker particle method (SEMP) to three-phase flow. Three compressible fluid phases (with different material parameters) are modelled using a one-field approach where the phases are tracked using the Lagrangian marker particle method. The marker particle method allows for severe topological changes in the fluid-fluid interfaces, whilst the spectral element method employs high-order interpolating polynomials and therefore, ensures a high degree of accuracy.

The paper is motivated by bioengineering applications and presents novel results for low inertia bubble collapse near a fluid-fluid (biological) interface. A range of fluid parameter values and geometric configurations are considered to assess the behaviour of the numerical method and the effect of fluid parameters on bubble-interface dynamics.

The final configuration presented models single cell-bubble interaction, where it is shown (for the first time) that the non-localised disruption to the cell membrane observed experimentally may be purely mechanical in nature, arising due to rapid propagation of normal and shear stresses through the interior of the cell and along the cell membrane during nearby bubble oscillation.

It is hoped that this article will be useful to those looking to model three-phase Newtonian bubble problems, and will pave the way for more representative computational studies of (micro)-bubble enhanced sonoporation (drug delivery).

I look forward to hearing from you in due course.

Yours Sincerely,

Christopher F. Rowlatt